The Florida State University
DigiNole Commons

4-22-2010

Application of Quantum Dots in Gene Therapy

Laura F. Barnes
Florida State University, Laura.Barnes@usafa.edu

Follow this and additional works at: http://diginole.lib.fsu.edu/etd

Recommended Citation

THE FLORIDA STATE UNIVERSITY

COLLEGE OF ARTS AND SCIENCES

APPLICATIONS OF QUANTUM DOTS IN GENE THERAPY

By

LAURA F. BARNES

A Thesis submitted to the
Department of Chemistry and Biochemistry
in partial fulfillment of the
requirements for the degree of
Master of Science

Degree Awarded:
Summer Semester, 2010

The members of the committee approve the thesis of Laura F. Barnes defended on April 23, 2010.

                              _____
                              Proff Geoffrey Strouse
                              Professor Directing Thesis

                              _____
                              Proff Timothy Logan
                              Committee Member

                              _____
                              Proff Brian Miller
                              Committee Member

The Graduate School has verified and approved the above-named committee members

ACKNOWLEDGEMENTS

I would like to thank Professor Geoff Strouse and Dr. Steve Yun for guiding me through these projects in the laboratory, in data analysis, and in writing this thesis.

I would like to thank Steve Hira and Chris Ridel for taking microscope pictures of my cells.

I would like to thank my husband, Robby, and my daughter, Samantha, for supporting me as I've finished this thesis.

TABLE OF CONTENTS

LIST OF TABLES

LIST OF FIGURES

ABSTRACT

Gene therapy is a rising field and requires multifunctional delivery platforms in order to overcome the cellular barriers. Quantum dots (QDs) provide a optically fluorescent and biocompatible surface to act as a multifunctional delivery platform for gene therapy. The objective of this research is to manipulate the surface of quantum dots for use in gene therapy. The first goal was to make the QDs water soluble and therefore biocompatible. The second goal was to functionalize the surface of the QDs with plasmid DNA for direct use in gene therapy. This approach uses chemoselective coupling chemistry between an InP/ZnS quantum dot (QD) and linker DNA (DNA_{linker}) to control the timing of protein expression. Linear DNA (IDNA), containing the CMV promoter and DsRed-Express gene, was condensed on the surface of the QD-$DNA_{linker.}$ Optical and flow cytometry analysis of the DsRed-Express expression after transfection of the QD-IDNA into CHO cells shows a delayed protein expression for both coupling chemistries compared to naked IDNA. It is also clear that the protein expression form the QD-*S*-IDNA turns on quicker than the QD-*NH*-IDNA. We believe the protein expression delay is due to the site of coupling between the QD and DNA_{linker} and its affect on the IDNA packing strength. The S-DNA_{linker} is believed to couple by direct exchange at the vertices of the QD whereas the NH-DNA_{linker} couples through a condensation reaction to the facets. The delay in protein expression reflects the delayed exchange rate at the facets over the vertices. The ability to control the coupling chemistry and timing of release from the QD surface suggests a mechanism for dose control in transient gene therapeutics, and show QD delivery approaches are ideal candidates for multifunctional, targeted, drug carrying platforms that can simultaneously control dosing. The third goal of this research was to functionalize the surface of the QDs with the HIV cell penetrating peptide, TAT, and study its affects on QD internalization as well as toxicological affects within the cells. Tracking of the cellular uptake of these QDs by optical microscopy shows rapid, diffuse accumulation of both 10 % TAT and 100 % TAT passivated QDs throughout the cytosol of the cells. Toxicity studies were conducted by flow cytometry to investigate the effects of these materials on apoptosis, necrosis, and metabolic damage in Chinese Hamster Ovary (CHO) cells.

These studies suggest toxic effects of the cell penetrating QDs are dependent on the amount of CAAKA-TAT used on the surface of the QD as well as the concentration of QD added. These observations aid in the use of QDs as self transfecting, nano delivery scaffolds for drug or gene therapy.

CHAPTER 1

INTRODUCTION

The ability to deliver siRNA, antisense DNA, or linearized genes into mammalian cells while controlling the dosing level and timing of gene expression represents a transformative goal for next-generation gene therapeutics.[1-5] The use of nucleic acid-based therapeutics has shown great promise in treating diseases, yet it faces many obstacles in designing appropriate platforms for packaging the nucleic acids. These packages must avoid immunological cellular response and promote cell specific targeting, efficient cellular transfection, endosomal escape, and nuclear transcription.[1-10] Viral vectors and non-viral vectors such as cationic polymers, liposomes, and inorganic nanoparticles have been shown to be effective at manipulating protein expression levels within a cell; however, many of these approaches exhibit toxic immunological effects, mutagenesis, and carcinogenesis.[1,3,11] Thus, it is essential these delivery platforms are designed with multifunctional components to address each of these areas when attempting gene therapy.

One non-viral approach that has promise is the use of photoluminescent quantum dots (QDs). Quantum dots (QDs) are optically stable, wavelength tunable, and easily integrated with biological components.[12-56] QDs used as delivery platforms are optically traceable and capable of tethering multiple bio-ligands, such as DNA, RNA, cell penetrating peptides (CPPs), and nuclear localization sequences (NLS), without disturbing the biological function (Figure 1).[12-56] The potential for QD use in biomedical applications is clear when coupled to the recent observation that QDs in the < 6 nm size regime can be excreted through renal pathways.[33,57] Adaptation into the biological environment and use in bio medical therapeutics is clearly the next step.

Already there is a wealth of literature demonstrating the viability of QD delivery via endosomal uptake with subsequent release of the nucleic acid package either via pH, enzymatic, or glutathione (GSH) mediated release from the QD surface.[19,28,43,53,58-60] Although it is well established, GSH mediated release of thiols from a QD surface in an endosome provides an efficient pathway for gene release,[60-62] control of the dosing, or

timing of release is not well understood. Chemoselective appendage of the target nucleic acid in terms of both the chemistry and site of appendage may provide timing and dosage control.[4,60-62] Depending on the nature of coupling (electrostatic, antibody mediated, or covalent appendage to the organic passivating layer), the efficiency of gene expression thus can be controlled by limiting release from the QD surface.[59-63]

A)
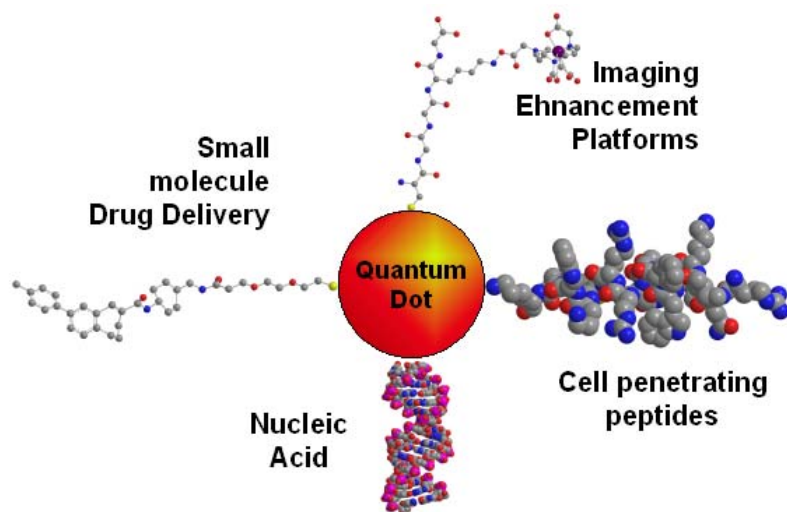
Figure 1: Surface modifications for the bio-functionalization of quantum dots include RNA, DNA, cell penetrating peptides, nuclear localization sequences, small drug molecules and imaging enhancing platforms.

There has also been an incredible amount of focus on cellular delivery mechanisms for the QD platforms. Different mechanisms for uptake have been explored, but of particular interest are CPPs.[5,64] CPPs are short (<30) arginine rich amino acid sequences that have a positive net charge enabling them to carry cargo through the cellular membrane and sometimes into the nucleus.[64-67] It is believed that CPPs carry their cargo through predominantly endocytotic pathways, however, there is evidence for direct translocation through the membrane as well.[66] Although CPPs have been traditionally used to carry biomolecules into cells, over the last decade they have

been used in conjunction with QDs for various purposes.[15-18,21,23-25,27,29-32,38-39,42,44-46,50-52,56]

While cellular toxicity from CPPs has been shown to be negligible,[64,66] studies show that toxicity of CPP-QD complexes are dependent on concentration and the type of attachment chemistry between the CPPs and QDs.[51] Additionally, there remains a real concern for some classes of QDs,[11,22,28,37,68] new QDs based on less toxic InP based fluorophores are finding increased interest.[69-71] As the III-V materials become more readily available, preliminary studies have begun to appear in the literature.[14,54] Choosing InP/ZnS over CdSe/ZnS QDs reflects not only the perceived lower toxicity, but also the added advantage of a smaller bandgap for InP, which allows smaller (< 4 nm), highly luminescent (~50% photoluminescent quantum yield) visible QDs to be utilized.[72-74]

Research Objectives and Summary of Chapters

The objective of this research is to manipulate the surface of quantum dots for use in gene therapy. The first goal was to make the QDs water soluble and therefore biocompatible. The second goal was to functionalize the surface of the QDs with plasmid DNA for direct use in gene therapy. Encompassed in this goal was also a study of how different surface interactions affect DNA coupling and protein expression. The third goal of this research was to functionalize the surface of the QDs with the cell penetrating peptide, TAT, and study its affects on QD internalization as well as toxicological affects within the cells.

The methods for synthesizing and characterizing QDs are briefly discussed in this Chapter Two of this manuscript. The unique optical properties of quantum dots as well as the predictable surface chemistry of a ZnS shell make them desirable for many applications. The ability to tune the frequency of photon emission allows for easy experimental design for optical and fluorescence analysis techniques. A simple surface exchange chemistry is described to produce water soluble QDs that can be used for biological applications. The characterization data suggests that the quantum yield is affected by water solubility; however, the QDs maintain a stable emission with enough intensity for use in such applications.

Chapter Three of this manuscript investigates the dependence of the nucleic acid and QD surface packing strategy to control the timing of intracellular expression of a fluorescent protein (DsRed-Express) delivered on 3.5 nm InP/ZnS and CdSe/ZnS core-shell QDs into Chinese Hamster Ovary (CHO) cells (Figure 2A). Quantum dot scaffolds were prepared on both InP/ZnS-MUA and CdSe/ZnS-DHLA QDs by two methods. The first was a direct exchange at the reactive edge and vertex sites on the QD surface displacing the acid passivant layers with a 5'thiol phosphoramidate modified linker dsDNA. The second was a condensation reaction at the QD facet sites by a 5'amine phosophoramidate modified linker dsDNA to the acid head group on the passivant layers. A linearized DsRed-Express gene plus CMV promoter (lDNA) was aggregated around these QD scaffolds through a phosphate backbone interaction with free Zn^{2+} ions.

Tracking DsRed-Express expression by optical microscopy and flow cytometry after transfection of the QD-lDNA assemblies provides direct evidence that aggregate strength controls the timing of expression of the gene, not the level of protein expression in live cell experiments. The data suggests that QD-lDNA strength is dictated not only by the chemoselective coupling of the short linker dsDNA sequence, but also the original passivant layer on the QD. The observation that passivant layers and coupling chemistry provides a mechanism to manipulate gene release from a QD surface may lead to a mechanism for dose control in transient gene therapeutics, and show QD delivery approaches are ideal candidates for multifunctional, targeted, drug carrying platforms that can simultaneously control dosing. One possibility would be to ligate the DsRed lDNA to the linker on the QD so that release of the DNA and expression of DsRed-Express could be controlled by pH changes that facilitate release from the QD (Figure 2B).

Chapter four of this manuscript investigates the use of the widely used cell penetrating peptide, TAT, derived from the HIV-1 transactivating factor,[66] to passivate the surface of 3.5 nm InP/ZnS and CdSe/ZnS core-shell QDs and monitor the effects on cellular uptake and metabolic toxicity in varying cell types. The cell penetrating QDs were prepared through surface ligand exchange with either 90 % of the neutral peptide CAAKA plus 10 % of the positively charged peptide CAAKATAT or 100 % of

CAAKATAT. Tracking of the cellular uptake of these QDs by optical microscopy shows rapid, diffuse accumulation of both the 10 % TAT and 100 % TAT passivated QDs throughout the cytosol of the cells. Toxicity studies were conducted by flow cytometry to investigate the effects of these materials on apoptosis, necrosis, and metabolic damage in Chinese Hamster Ovary (CHO) cells. These studies suggest toxic effects of the cell penetrating QDs are dependent on the amount of CAAKATAT used on the surface of the QD as well as the concentration of QD added. These observations aid in the use of QDs as self transfecting, nano delivery scaffolds for drug or gene therapy.

Figure 2: A) Experimental design for QD aggregation with linearized pCMV-DsRed-Express fragments for transfection and expression in CHO cells. B) Experimental design for QD attachment to linearized pCMV-DsRed-Express for transfection and expression in CHO cells.
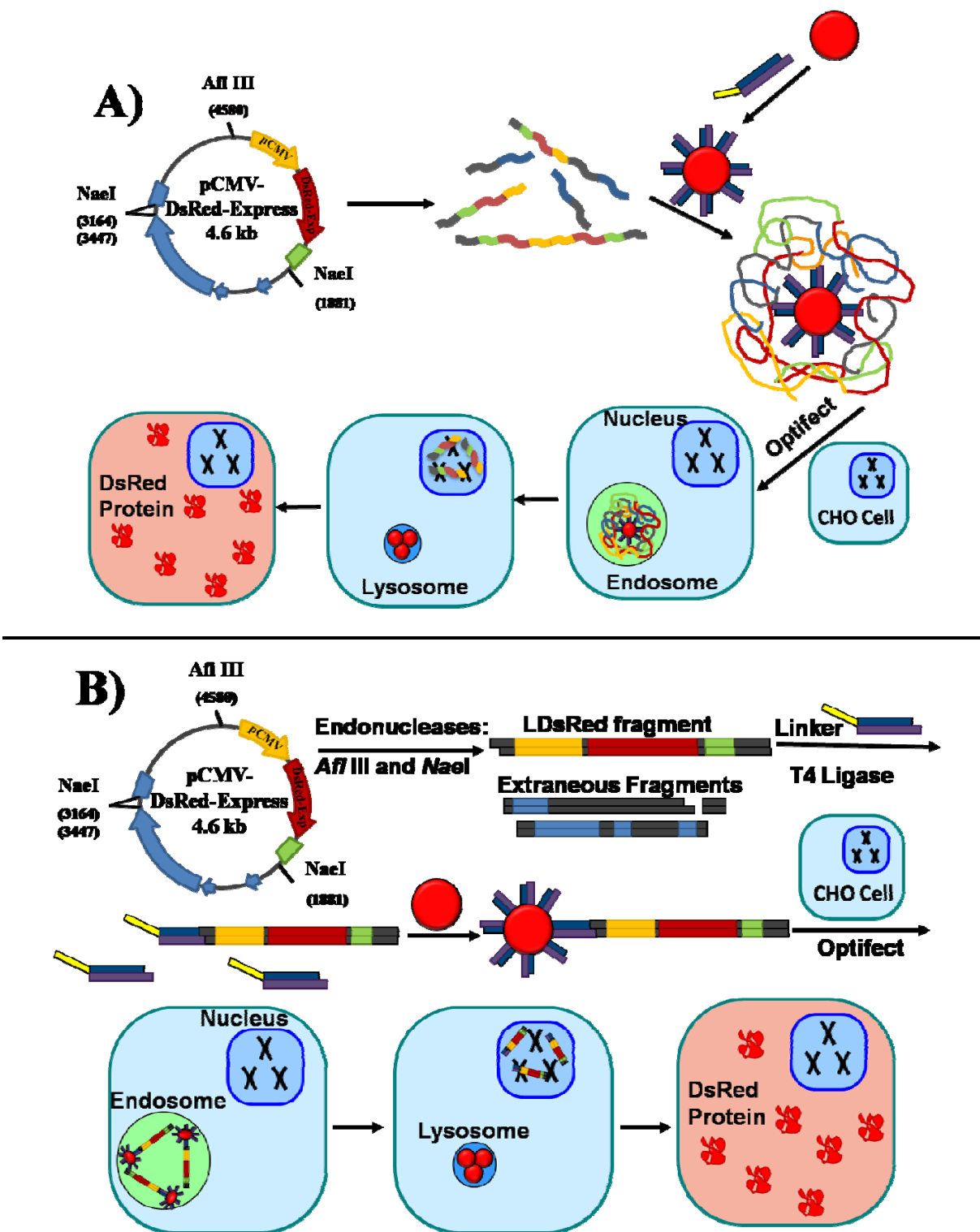
CHAPTER 2

WATER SOLUBLE QUANTUM DOT SYNTHESIS AND CHARACTERIZATION

Quantum dots are unique and widely popular semiconductor nanocrystals with inherent, tunable emission properties that make them suitable for a wide range of applications. QDs are typically composed of materials from the periodic groups of II-VI, III-V, or IV-VI and range in size from 2-10 nm.[72-75] Transmission electron microscopy (TEM) images of InP/ZnS (A-1) and CdSe/ZnS (B-1) QDs are shown in Figure 3 at approximately 5 nm. It is the small size of QDs that allows for their tunable emission properties. In a bulk material, an electron can be excited from the valence band into the conduction band. When the electron relaxes back into the valence band, it releases a photon with a frequency that is equal to the energy difference between the two bands, known as the Exciton Bohr Radius. For a given bulk material, this radius is able to extend to its full limit and therefore the energy of the photon emission is constant. Quantum dots, however, are smaller than the bulk material's Exciton Bohr Radius and fall into what is known as quantum confinement. The energy of the releasable photon is no longer dictated by the size of the Exciton Bohr Radius, but is now dictated by the physical size of the QD crystal.[72-75] Therefore, by changing the size of the QD by a few atoms, the emission wavelength can be tuned with great precision. QDs emission ranges from UV-visible to near IR region of the optical spectrum depending on the materials used.[22,72-75] Figure 3 shows images of varying sizes of InP/ZnS (A-1) and CdSe/ZnS (B-1) QDs that are photoluminescent at different frequencies after excitation by UV light. The smaller QDs on the left emit at lower frequencies (blue/green) while the larger QDs on the right emit at higher frequencies (orange/red).

Since their first description in 1982,[61,76] many synthetic methods and post-synthetic modifications have emerged in order to tailor the QDs for specific applications.[77-82] Although the core components, such as CdSe and InP dictate the specific optical properties of the QDs, shelling techniques using ZnS work to stabilize the QDs against oxidation. Typically, the shells are grown around the surface of a core

crystal. Although the core synthesis and shell growth are accomplished in a nonpolar solvent, the solubility of the nanocrystal is controlled by surface ligands bound to sulfur atoms on the ZnS shell. Figure 3C shows a three-dimensional cross-section of a CdSe/ZnS QD with hydrophobic surface ligands.
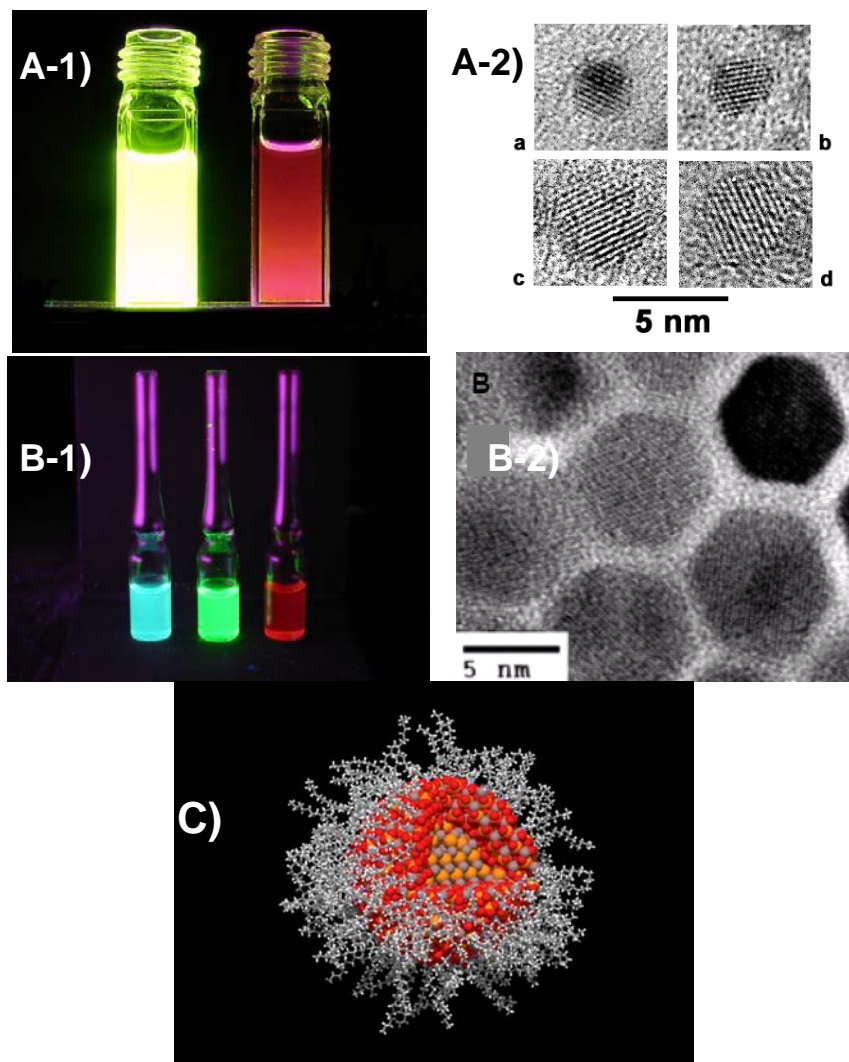
Figure 3: A-1) Photoluminescent image of InP/ZnS QDs. A-2) TEM images of InP/ZnS QDs. B-1) Photoluminescent image of CdSe/ZnS QDs. B-2) TEM image of CdSe/ZnS QDs. C) Three dimensional depiction of a CdSe/ZnS QD cross-section. The cross section shows the inner core of Cd and Se atoms surrounded by a shell of Zn and S atoms. The surface ligands bind to sulfur atoms in the shell surrounding the QD.

Quantum Dot Synthesis

The InP/ZnS QDs were synthesized in-house using proprietary microwave technology.[72-73] The purpose of this chapter is to make these pre-synthesized QDs water soluble through ligand exchange chemistry. The CdSe/ZnS QDs used in this work were purchased from Evident Technologies (evidot©540, 3.5 nm). Although the evidots are ZnS shelled, it is suspected that there is some sort of polymer coating around the shell. These CdSe/ZnS were used as a commercial baseline for comparison within this manuscript.

**Water Solubility Ligand Exchange and Characterization.**

Water soluble 3.5 nm InP/ZnS QDs[73] were prepared by ligand exchange of hexadecylamine (HDA) capped QD, by mercapto undecanoic acid (MUA) as described previously (Figure 4A).[83] Specifically, a solution of MUA (100 mg) in toluene (6 mL) was added to the HDA capped QD (5 mg) dissolved in 100 μL of toluene and allowed to stir at room temperature under N_2 for 36 hrs. The solution was centrifuged (20 min) to pellet the MUA-QD, washed with toluene, and re-pelleted. To ensure complete recapping by MUA, the pelleted QD was suspended in DMF (10 mL) with sonication, MUA (10 mg) was added, and the solution was allowed to stir at room temperature under N_2 overnight. Na_2CO_3 (100 mg) was added to the MUA-QD and allowed to stir overnight to deprotonate the –COOH functional groups. The solution was centrifuged for 20 min separately pelleting the QD and excess Na_2CO_3 due to their respective solubility in DMF. The QD pellet was resuspended in a minimum of DMF to remove the excess Na_2CO_3. The QD solution was washed with DMF two times by removing the DMF supernatant after centrifugation and resuspending the pellet in fresh DMF. After the final wash, the MUA-QD pellet was resuspended in potassium phosphate buffer (KPB) (50 mM, pH 7.2) with vortexing and sonication. The QDs were then precipitated with ethanol to remove unwanted organic contaminants and solubilized in potassium phosphate buffer (50 mM, pH 7.2).

The Evidot CdSe/ZnS QDs underwent the same water soluble ligand exchange process as the InP/ZnS QDs. The only difference was the use of dihydrolipoic acid (DHLA) on the CdSe/ZnS QD surface instead of MUA. MUA attaches to the ZnS shell through a single thiol bond whereas the DHLA attaches through dual-thiol bonds (Figure

4). The DHLA and MUA ligands work equally well to make the QDs water soluble as shown in Figure 4. The image in Figure 4B shows biphasic solutions of CdSe/ZnS in toluene and water. The hydrophobic CdSe/Zns on the left is solubilized in the toluene. After the ligand exchange with DHLA, the CdSe/ZnS becomes hydrophilic and is solubilized in the water on the right.   Water solubility was also confirmed by gel electrophoresis in a 1 % agarose gel for the InP/ZnS-MUA QDs (Figure 4C) and the CdSe/ZnS-DHLA QDs (Figure 4D).
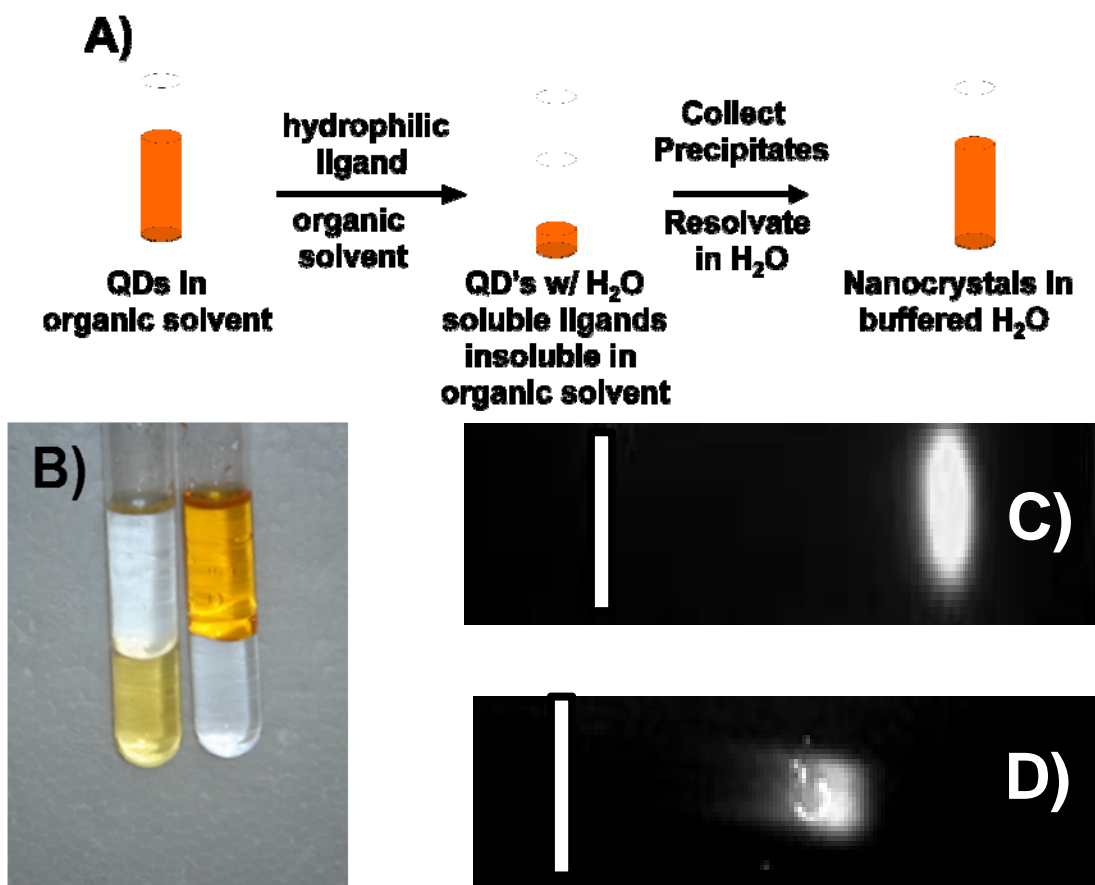
Figure 4: A) Procedural schematic to make QDs water soluble through ligand exchange. B) Before and after images of CdSe/ZnS in biphasic solutions. The hydrophobic CdSe/ZnS is solubilized in toluene on the left. The hydrophilic CdSe/ZnS is solubilized in water on the right. C) Gel electrophoresis (1 %) of MUA passivated InP/ZnS. D) Gel electrophoresis (1 %) of DHLA passivated CdSe/ZnS. White lines in C & D mark the starting wells.

CdSe/ZnS

A)

InP/ZnS

B)

C) −30 %

D) −14 %
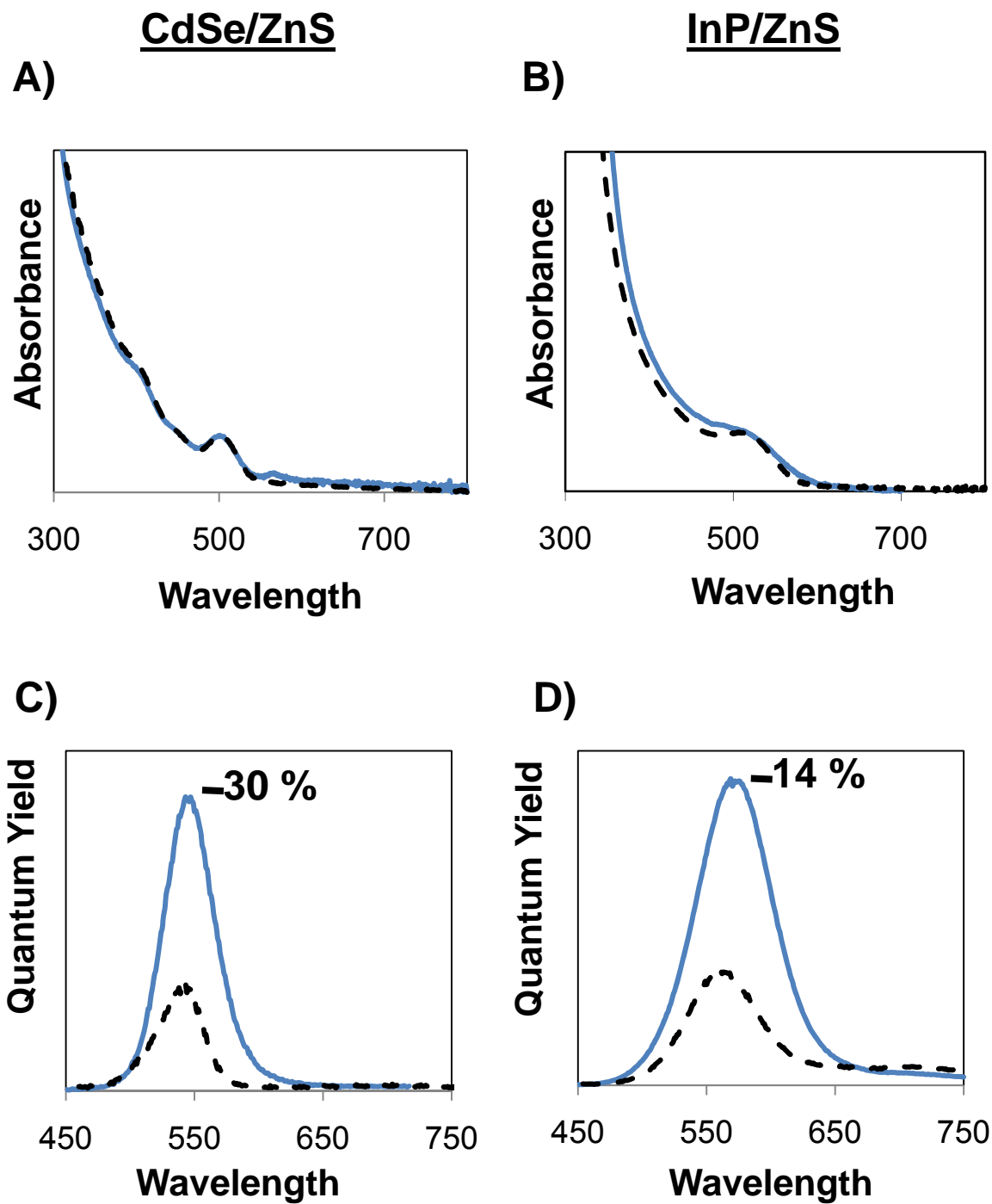
Figure 5: A) Absorbance spectra of CdSe/ZnS. B) Absorbance spectra of InP/ZnS. C) Emission spectra of CdSe/ZnS. D) Emission spectra of InP/ZnS. In A-D, the solid blue line represents QDs solubilized in toluene and the dashed black line represents QDs solubilized in phosphate buffer.

Further characterization of the water soluble QDs was achieved by optical absorption and photoluminescence analysis (Figure 5). Absorbance data for the CdSe/ZnS (5A) and InP/ZnS (5B) QDs indicates no change in the spectral manifold after ligand exchange with the DHLA and MUA respectively. There is, however, a noticeable loss of quantum yield in both cases. According to Evident, the quantum yield of the CdSe/ZnS solubilized in toluene is 30 %. As shown in Figure 5C, the quantum yield of the water soluble CdSe/ZnS-DHLA is approximately one third of the original QD. The same loss of quantum yield is seen for InP/ZnS-MUA (5D). This loss of photoluminescent intensity is most likely due to surface oxidation during the ligand exchange; however the exact mechanism is not known. Despite the low quantum yields of the water soluble QDs, the photoluminescence in KPB remains stable at 4 ^{o}C for greater than six months.

Conclusions

The unique optical properties of quantum dots as well as the predictable surface chemistry of a ZnS shell make them desirable for many applications. The ability to tune the frequency of photon emission allows for easy experimental design for optical and fluorescence analysis techniques. The simple surface exchange chemistry demonstrated here provides for water soluble QDs that can be used for biological applications. Although the quantum yield is affected by water solubility, the QDs maintain a stable emission with enough intensity for use in such applications, as shown in Chapters 3 and 4 of this work.

CHAPTER 3

GENE THERAPY USING A QUANTUM DOT SCAFFOLD

This chapter investigates the dependence of the nucleic acid and QD surface packing strategy to control the timing of intracellular expression of a fluorescent protein (DsRed-Express) delivered on 3.5 nm InP/ZnS and CdSe/ZnS core-shell QDs into Chinese Hamster Ovary (CHO) cells (Figure 6). Quantum dot scaffolds were prepared on both InP/ZnS-MUA and CdSe/ZnS-DHLA QDs by two methods. The first was a direct exchange at the reactive edge and vertex sites on the QD surface displacing the acid passivant layers with a 5'thiol phosphoramidate modified linker dsDNA. The second was a condensation reaction at the QD facet sites by a 5'amine phosophoramidate modified linker dsDNA to the acid head group on the passivant layers. A linearized DsRed-Express gene plus CMV promoter (lDNA) was aggregated around these QD scaffolds through a phosphate backbone interaction with free Zn^{2+} ions.

EtOH
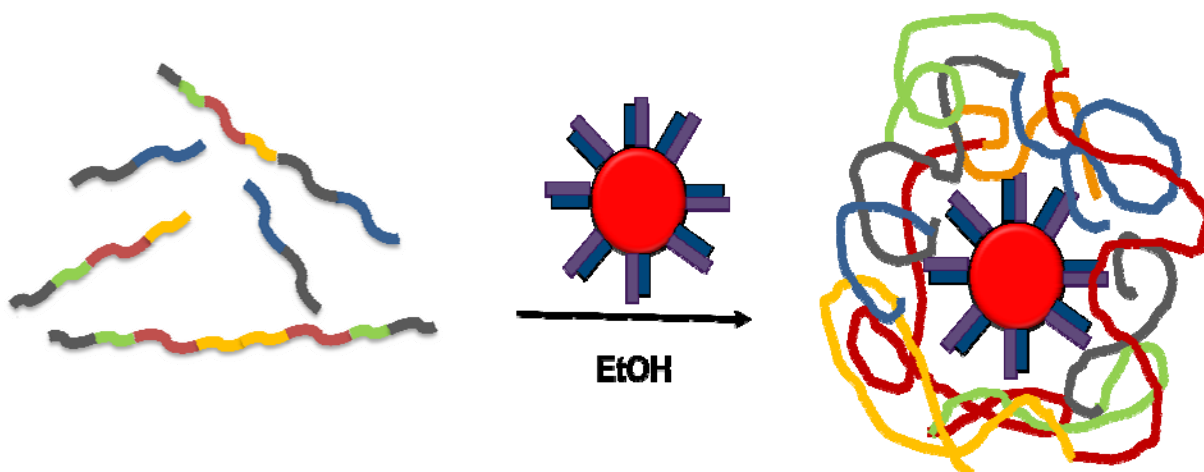
Figure 6: Schematic showing aggregation of DNA around a DNA-functionalized QD.

Tracking DsRed-Express expression by optical microscopy and flow cytometry after transfection of the QD-lDNA assemblies provides direct evidence that aggregate strength controls the timing of expression of the gene, not the level of protein

expression in live cell experiments. The data suggests that QD-lDNA strength is dictated not only by the chemoselective coupling of the short linker dsDNA sequence, but also the original passivant layer on the QD. The observation that passivant layers and coupling chemistry provides a mechanism to manipulate gene release from a QD surface may lead to a mechanism for dose control in transient gene therapeutics, and show QD delivery approaches are ideal candidates for multifunctional, targeted, drug carrying platforms that can simultaneously control dosing.

Materials and Methods

pCMV-DsRed-Express lDNA preparation. Linearized DNA (lDNA) was prepared by cutting the pCMV-DsRed-Express Vector (4.6 kb; Clontech) at restriction sites for AflIII and NaeI following manufacturer's protocols (New England BioLabs). The vector contains three restriction sites for NaeI (Figure 7A), resulting in blunt ended fragments of 1283 bp, 1133 bp, and 238 bp as confirmed in the 1 % agarose gel in Figure 7C. The vector containes one restriction site for AflIII (Figure 7A), resulting in a 4 base overhang sticky end as confirmed in the 1 % agarose gel in Figure 7C. Treatment with both endonucleases yields a linear 1981 bp DNA fragment containing the pCMV-DsRed-Express gene with a 3' blunt end and a 5', 4 base overhang sticky end. Proper vector digestion was confirmed on a 1 % agarose gel (Figure 7B).

Double stranded synthetic linker DNA preparation. A short double stranded synthetic DNA linker[84] was prepared for attachment to the QD surface. The synthetic duplex consisted of a 33 bp single stranded DNA (ssDNA) annealed to a complementary 29 bp ssDNA creating a 4 base overhang. The 33 bp synthetic DNA strand contained a 5'-C_6 modification off the phosphate backbone (5' C_6 thiol (*HS*-DNA$_{linker}$) or 5'-C_6 amine (*NH$_2$*-DNA$_{linker}$)) to allow attachment to the QD surface as shown in Figure 8. To verify and quantify the assembly of the DNA linker on the QD, the 33 bp synthetic strand was prepared with an AF594 modification off the 15th bp T-base[81] for use in the FRET experiments described below.

QD-*S*-DNA$_{linker}$ (direct thiol coupling) and lDNA aggregation. To couple the thiol DNA linker (*HS*-DNA$_{linker}$) by MUA or DHLA ligand exchange, the *HS*-DNA$_{linker}$ was fully reduced using dithiothreitol (10mg/ml DTT 3h) and passed through a NAP[th] 5 column to remove excess DTT and DNA linker prior to coupling to the QD. The purified

HS-DNA$_{linker}$ was added in excess to the QD in potassium phosphate buffer (50 mM, pH 7.2) and agitated for 3-4 h. The solution was then placed at 4 ^{o}C for 72 h. The lDNA was added to the the QD-*S*-DNA$_{linker}$ in a 1:3 molar ratio and aggregated through dehydration by ethanol precipitation (50% V/V EtOH/KPB, 25 ^{o}C). The coupling was quantified by absorption spectroscopy using a dye labeled linker strand. The coupling and aggregation were verified on a 1 % agarose gel.

QD-*NH*-DNA$_{linker}$ (indirect amide coupling) and lDNA aggregation. To covalently couple the amine DNA linker (*NH$_2$*-DNA$_{linker}$) to the acid passivated QD via amide formation, the passivant shell was activated by the addition of N-hydroxysulfosuccinimide (NHSS) (100 μL, 1 mg/mL) and N-(3-dimethylaminopropyl)-N-ethylcarbodiimide hydrochloride (EDC) (10 μL, 10mg/mL) in potassium phosphate buffer (50 mM, pH 7.2), and agitated for 3-4 h. The *NH$_2$*-DNA$_{linker}$ was passed through a NAPth 5 column for purification and added in excess to the QD solution. The solution was agitated for 3-4 h and placed at 4 ^{o}C for 72 h. The lDNA was added to the the QD-*NH$_2$*-DNA$_{linker}$ in a 1:3 molar ratio and aggregated through dehydration by ethanol precipitation (50% V/V EtOH/KPB, 25 ^{o}C). Purification and validation of coupling were carried out as described above.

Cell Transfection by QD-DNA$_{linker}$. The QD-lDNA complexes were transfected into Chinese Hamster Ovary (CHO) cells at 30 % confluence (~0.5 x 10^6 cells) in a 6-well plate or 35 mm live-cell imaging dish (Matteck Corp) using the transfecting cationic lipid Optifect according to manufacturer's protocols (Invitrogen). CHO cells were grown at 37 °C in Dulbeccos Modified Eagle's Medium (DMEM, Gibco) supplemented with 10 % non-essential amino acids, 10 % cosmic calf serum, 1 % antibiotics / antimycotics, and 0.1 % Gentamycin.

Optical detection of transient DsRed-Express expression. The cells were allowed to incubate for 24 h at 37 ^{o}C following transfection by QD-lDNA. The media was exchanged at the 24 h time point to remove Optifect and non-transfected QDs prior to analysis.   The level of intracellular expression for DsRed-Express was monitored by flow cytometry (30,000 events at 24 h, 48 h, and 72 h). Flow cytometry analysis was accomplished on a BD FACS Canto II with 488 nm excitation and detection on a PE-A filter set (585/42). The transfected cells were washed with TBS, trypsinized (TrypLE,

Gibco), resuspended in media (10^6 cells/mL), and analyzed by flow cytometry against non-transfected CHO cells as a negative control to determine the positive threshold. Complimentary wide field microscopy images on a Nikon T2000E C1SI spectral confocal microscope were obtained at 24 h, 48 h, and 72 h, to correlate the internalization of the QD-lDNA complex, the long-term emissivity of the QD, and the level of DsRed-Express expression in the cells.
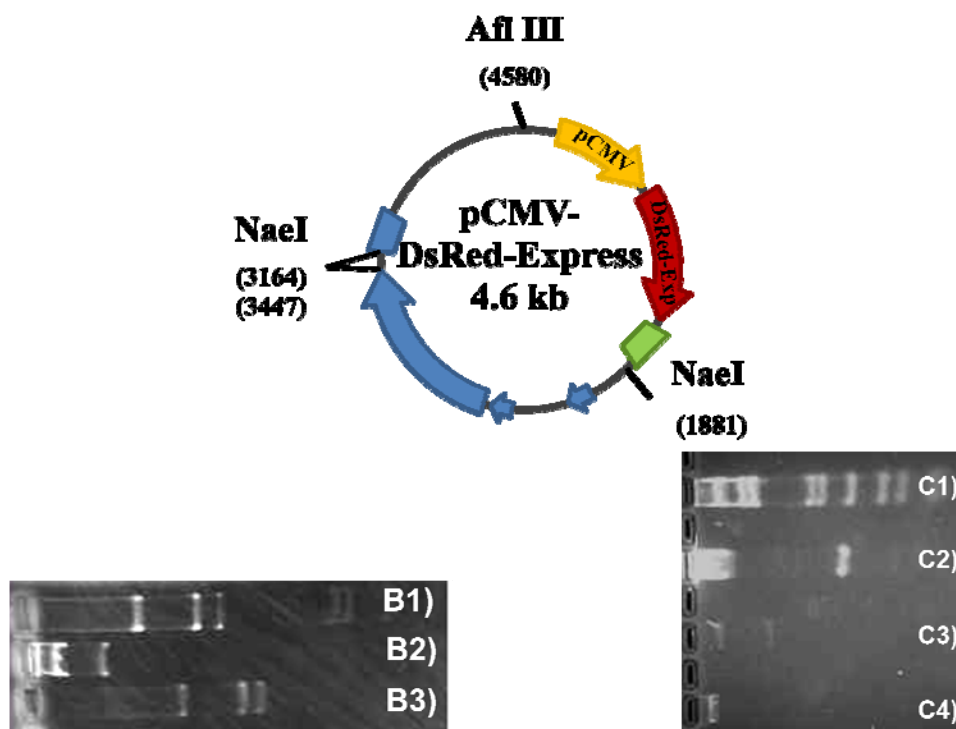
Figure 7. A) Schematic of pCMV-DsRed-Express showing endonuclease sites for AflIII and NaeI. B) Image of 1 % agarose gel showing (B1) pGEM ladder. The bands from left to right represent 2977 bp, 1799 bp, 1509 bp, 724 bp, and 676 bp. (B2) pCMV-DsRed-Express. The left band represents circular plasmid and the right band represents supercoiled plasmid. (B3) pCMV-DsRed-Express cut with AflII and NaeI. The bands from left to right represent the 1941 bp, 1283 bp, and 1133 bp segments of the plasmid. The small 283 bp fragment is not shown on the gel. C) Image of 1 % agarose gel showing (C1) pGEM ladder. The bands from left to right represent 2977 bp, 1799 bp, 1509 bp, 724 bp, 676 bp, 517 bp, 396 bp, 325 bp, and 244 bp. (C2) pCMV-DsRed-Express. The left band represents circular plasmid and the right band represents supercoiled plasmid. (C3) pCMV-DsRed-Express cut with NaeI. The left band represents the 1283 bp segment and the right band represents the 1133 bp segment. The small 283 bp fragment is not shown on the gel. (C4) pCMV-DsRed-Express cut with AflIII. The single band shows the plasmid has been cut once and is no longer supercoiled.

Results and Discussion

 Assembly of QD-IDNA.   A schematic of the QD-IDNA construct is shown in Figure 7. The DNA linker was designed with the desired functional group (5'-C$_6$ thiol (*HS*-DNA) or a 5'-C$_6$ amine (*NH$_2$*-DNA)) to allow for selective attachment to the QD. The functionalized DNA linkers were coupled to the surface of 3.5 nm MUA passivated InP/ZnS QDs and DHLA passivated CdSe/ZnS QDs using two distinct strategies. *HS*-DNA$_{linker}$ was used for direct ligand displacement of the acid passivant at the reactive edge/vertex sites (QD-*S*-DNA$_{linker}$, Figure 8A & 8C) and *NH$_2$*-DNA$_{linker}$ was used to directly couple to the acid layer through a condensation reaction of the DNA linker forming an amide linkage (QD-*NH*-DNA$_{linker}$, Figure 8B & 8D).   The 1.9 kb IDNA containing the CMV promoter and DsRed-Express gene was aggregated to the surface of these QD-DNA$_{linker}$ scaffolds.   The purified QD-DNA$_{linker}$ was structurally and fluorescently stable at 37 ^{o}C for greater than 96 h and at 4 ^{o}C for greater than six months.

 Characterization of the QD-DNA$_{linker}$ scaffold was accomplished through a FRET paring experiment of an InP/ZnS QD and an Alexa Fluor 594 dye at the 15th bp of the DNA linker. Figure 9 shows schematics of this pairing for the direct thiol linkage (A) and the indirect amide linkage (B). This paring allowed for quantitative analysis through the additive affects of absorption data.   It also allowed for qualitative analysis of the coupling event through the FRET exchange from the QD to the AF594.   Figure 9C shows the absorbance and emission of InP/ZnS and AF594 for reference.

 Quantitation of DNA$_{linker}$ appendage to the QD is evident in the absorption spectra shown in Figure 10 (B & E). An estimate of the loading level of DNA linker per QD can be obtained by comparing the optical spectra for a QD-DNA$_{linker}$ and AF594 sample in the absence of the QD. Comparison of the absorption intensity for the AF594 dye tag (ε_{587}=7.3x10^5 molL^{-1}cm^{-1}, Molecular Probes) to the first exciton (ε_{588} ~10^5 molL^{-1}cm^{-1}) for a 3.5 nm InP/ZnS QD reveal the ratio of coupling for the two are roughly 15:1 DNA$_{linker}$:QD for the *NH-* coupling and 5:1 for the *S-* coupling.
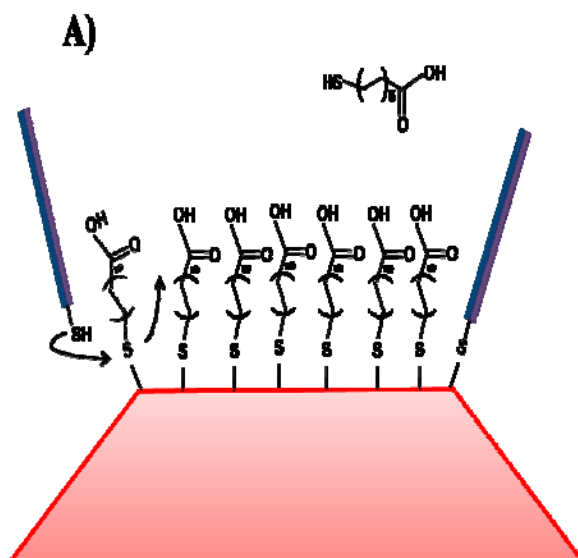
Direct Coupling　　　　　　　　　　**Indirect Coupling**
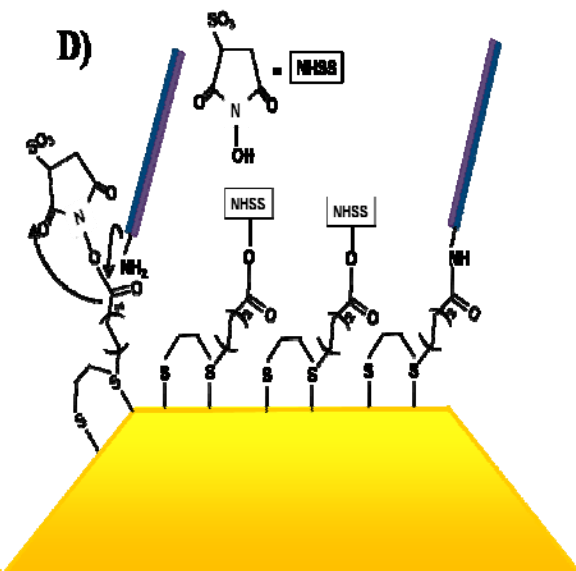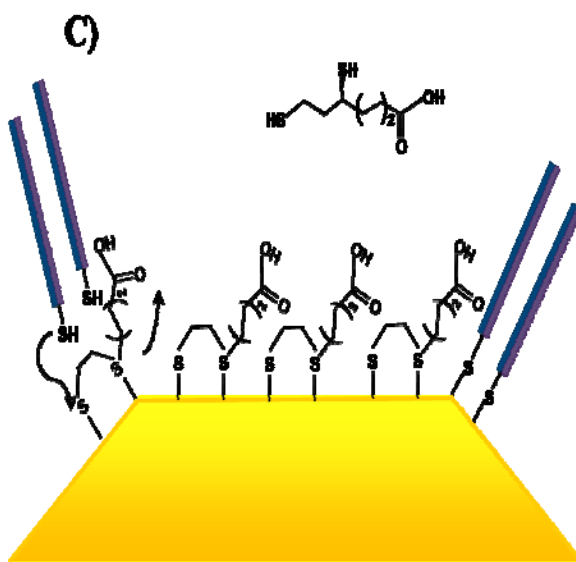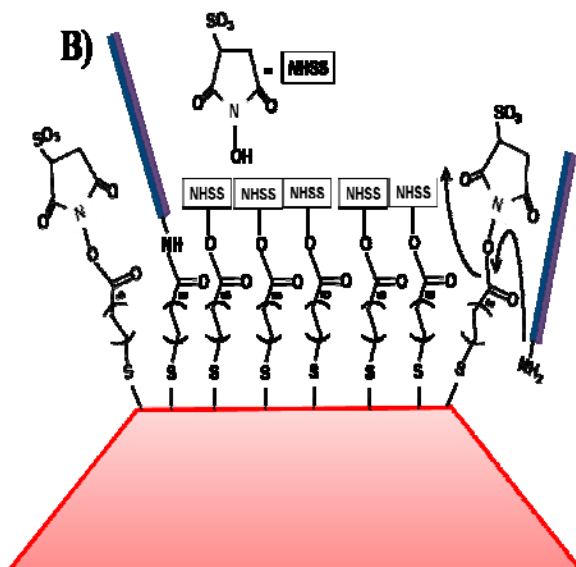
Figure 8. Coupling chemistry strategies used in this work. A) Direct thiol linkage between InP/ZnS-MUA and DNA$_{linker}$. B) Indirect condensation between InP/ZnS-MUA and DNA$_{linker}$. C) Direct thiol linkage between CdSe/ZnS-DHLA and DNA$_{linker}$. D) Indirect condensation between CdSe/ZnS-DHLA and DNA$_{linker}$. DNA linker is not to scale.
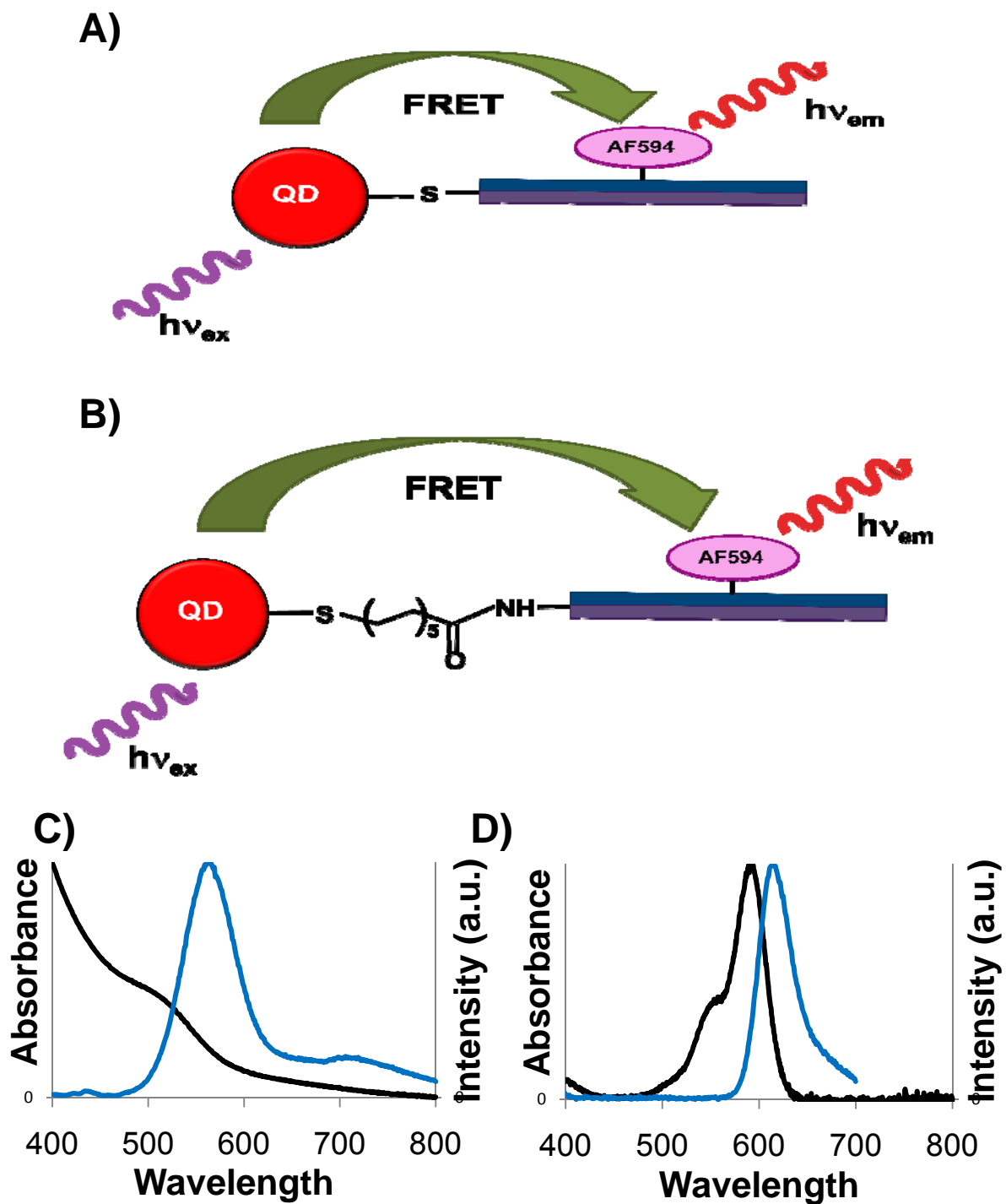
Figure 9: Schematics showing FRET between InP/ZnS and an AF594 dye labeling at the 15th bp of linear DNA attached through A) direct thiol linkage and B) indirect amide linkage. C) Absorbance (black) and emission (blue) spectra of InP/ZnS. D) Absorbance (black) and emission (blue) spectra of AF594.
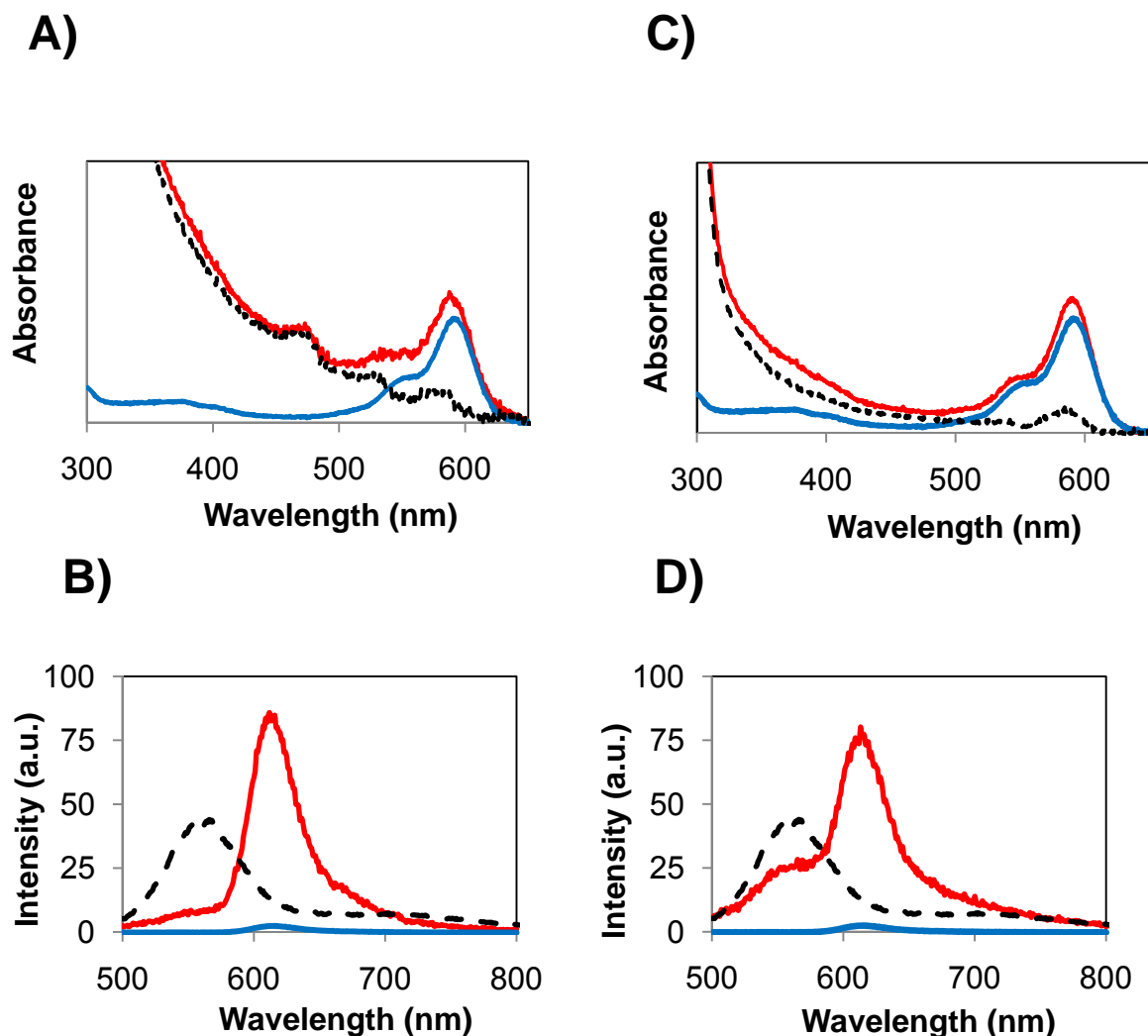
Figure 10. A) Absorption spectra for InP/ZnS-*S*-IDNA(AF594) (red), AF594 (blue), and InP/ZnS (black) extracted from InP/ZnS-*S*-IDNA(AF594) absorption. B) Fluorescence spectra (ex 460 nm) for InP/ZnS (black), AF594 (blue), and InP/ZnS-*S*-IDNA(AF594) (red) showing energy transfer from QD to AF594. C) Absorption data for InP/ZnS-*NH*-IDNA(AF594) (red), AF594 (blue), and InP/ZnS (black) extracted from InP/ZnS-*NH*-IDNA(AF594) absorption. D) Fluorescence spectra (ex460 nm) for InP/ZnS (black), AF594 (blue), and InP/ZnS-*NH*-IDNA(AF594) (red) showing energy transfer from InP/ZnS to AF594.

The most direct confirmation of direct coupling of DNA linker to the QD surface is provided by probing the assembly via an energy transfer assay.[19,77,80,82] In Figure 10 (C,F), a FRET assay (QD → AF594) confirms the DNA linker is bound to the QD. Excitation at 460 nm of the DNA linker construct which selectively excites the QD leads to strong AF594 emission. The AF594 excited at 460 nm in the absence of the QD

exhibits a decreased AF594 signal under identical concentration conditions. Following the QD emission confirms the first observation, as the QD emission in the absence of the AF594 is unquenched. Lack of coupling would result in no visible AF594 emission.

Evidence for aggregation of the IDNA to the QD-DNA$_{linker}$ is provided by inspection of the mobility changes observed in a 1 % agarose gel (Figure 11 A-D) between the QD and the QD-IDNA construct. The highly photoluminescent QD-IDNA exhibits strong retention of the band in the gel following IDNA aggregation for both linker coupling reactions. No free QD or IDNA are observed in the 1% agarose based upon analysis of the photoluminescent imaging of the QD or IDNA in the gel following ethidium bromide staining. The lack of free QD or IDNA in the gel is consistent with ethanol dehydration and purification of the QD-IDNA construct from impurities. Although no images of QD-IDNA were obtained, Figure 11E shows transmission electron miscroscope (TEM) images of Au-IDNA aggregates prepared in the same manner. The image shows DNA only aggregated around Au nanoparticles. This provides strong evidence for the same type of aggregation between QD and IDNA.

DsRed-Express protein expression. To analyze protein expression of the QD-IDNA construct, delivery of QD-*S*-IDNA and QD-*NH*-IDNA into the mammalian Chinese Hamster Ovary (CHO) cells was accomplished through the use of Optifect to promote endosomal uptake.[78-79] In Figure 12, no substantial time dependent differences for the InP/ZnS QD localization or degree of QD-IDNA uptake, based on the low resolution wide field images between 24 h and 72 h, are observed in the optical microscopy for the two independent coupling strategies. Spectral confocal deconvolution indicates the observed photoluminescence in the cells arises from InP/ZnS photoluminescence initially localized within an early or late endosomal package ($\geq$ 4 h, $\leq$ 24 h) (Figure 12A, 12C). Wide field imaging of the cells at 72 h indicate the QDs are still lodged within the endosomal/lysosomal package during the time course of the experiment (Figure 12B, 12D) implying no exocytosis of the QD-IDNA package or induced necrosis/apoptosis occurs. The images of CdSe/ZnS QD-IDNA uptake (Figure 13) indicate the same endosomal packaging, however, the CdSe/ZnS is no longer visible by 48 h. Although this might indicate that CdSe/ZnS is not as stable in the cell as InP/ZnS, it is probably due to differences in microscopy techniques. No evidence of nuclear membrane

association or nuclear internalization is observed in these images, as reported for other transfecting methods such as chitosan, poly(ethylenimine) PEI, and poly(propyl acrylic acid) (PPA).[19,85]
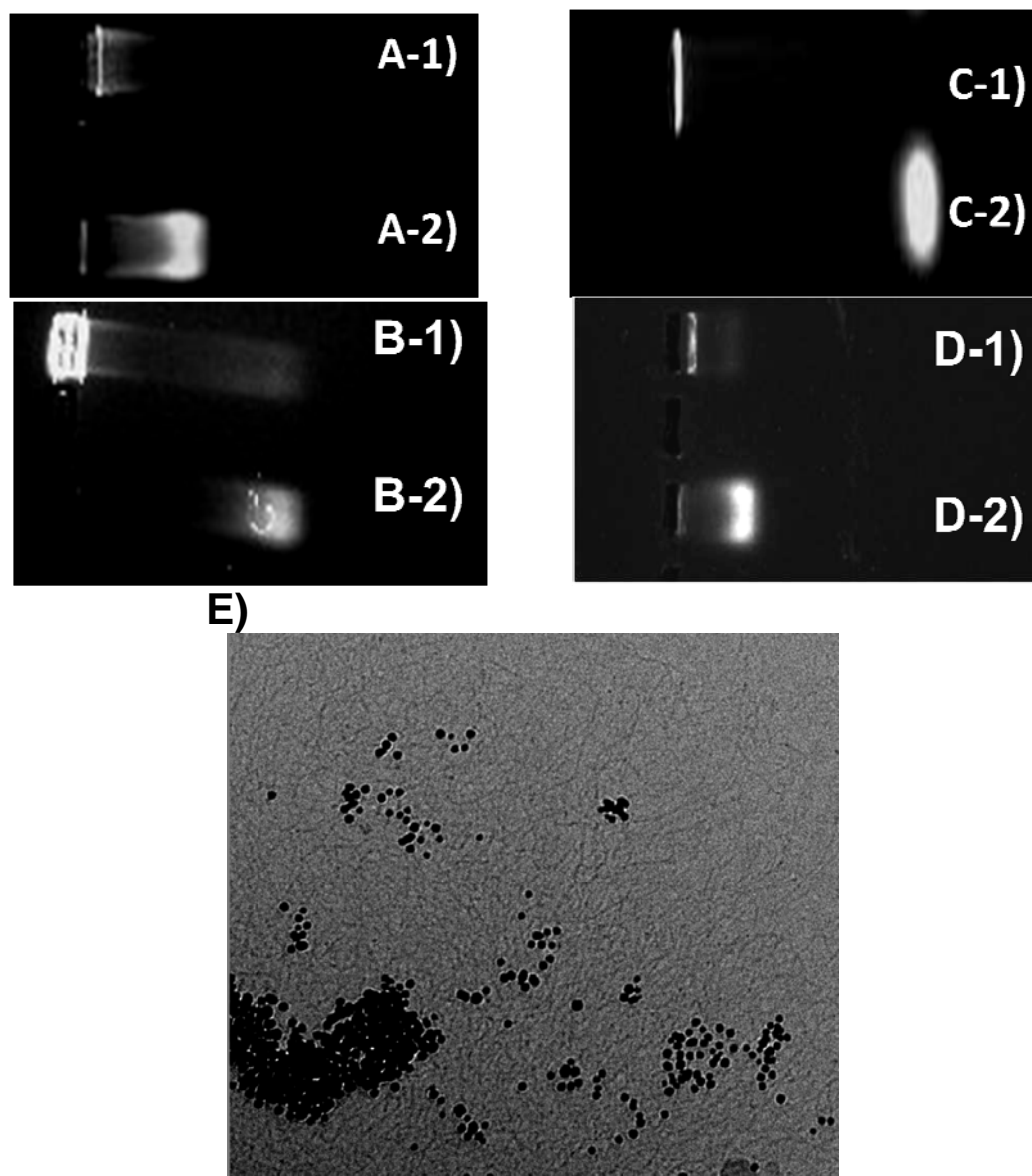
Figure 11. Gel electrophoresis of (A-1) direct *S*-IDNA coupling with InP/ZnS vs. (A-2) MUA passivated InP/ZnS; (B-1) direct S-IDNA coupling with CdSe/ZnS vs. (B-2) MUA passivated CdSe/ZnS; (C-1) indirect *NH*-IDNA coupling with InP/ZnS vs. (C-2) MUA passivated InP/ZnS; and (D-1) indirect NH-IDNA coupling with CdSe/ZnS vs. (D-2) MUA passivated CdSe/ZnS. E) TEM images of DNA aggregated around Au nanoparticles.
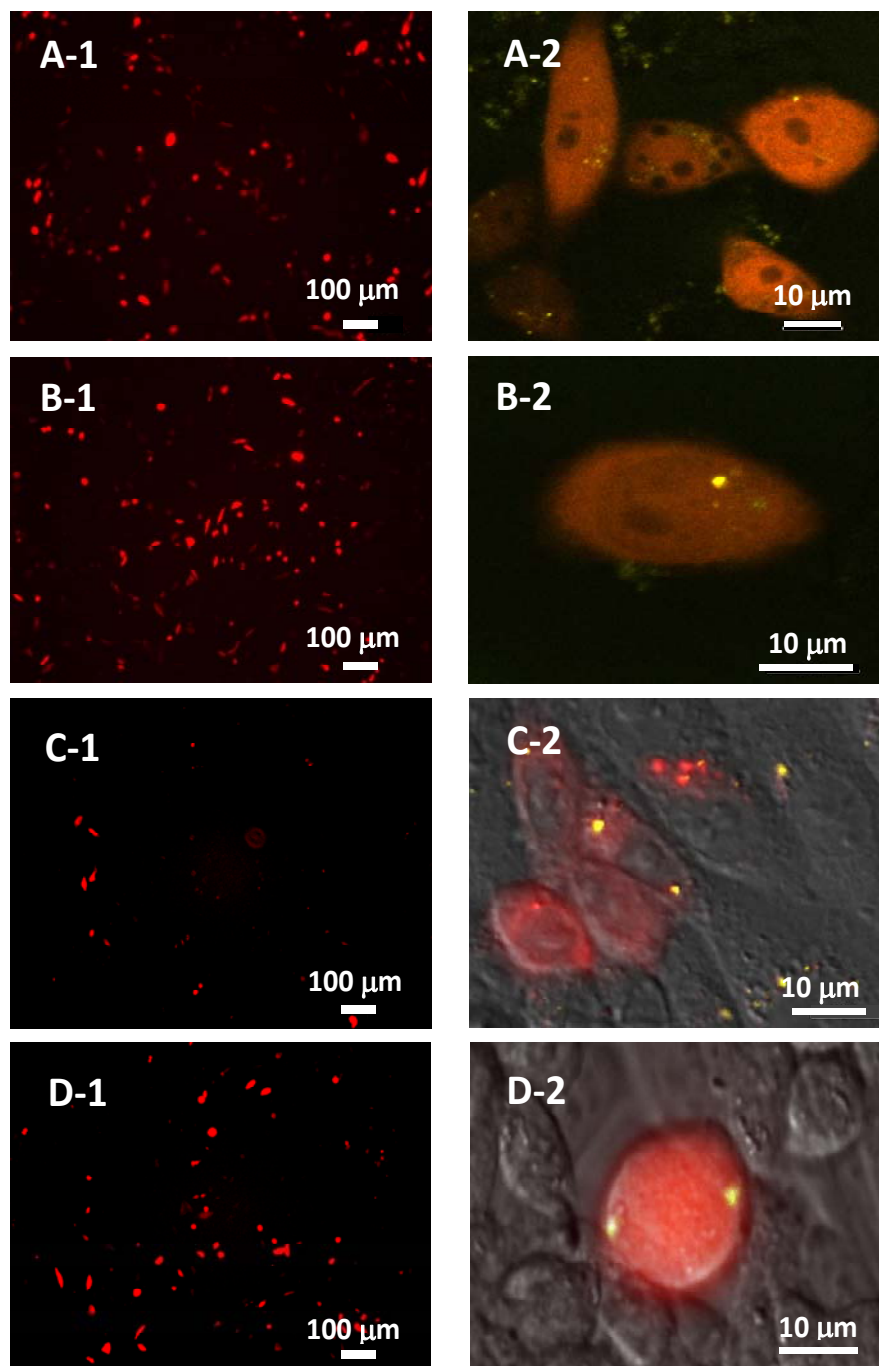
Figure 12. Microscopy images of CHO cells transfected with (A-B) InP/ZnS-*S*-IDNA and (C-D) InP/ZnS-*NH*-IDNA using Optifect. Images taken at 24 h (A, C) and at 72 h (B, D) post transfection. Image 1 are wide-field microscopy (10X) images, Image 2 are either Confocal spectral microscopy (40X) images (A-2, B-2) or wide-field microscopy (40X) images (C-2, D-2). All images are taken immediately following media exchange.
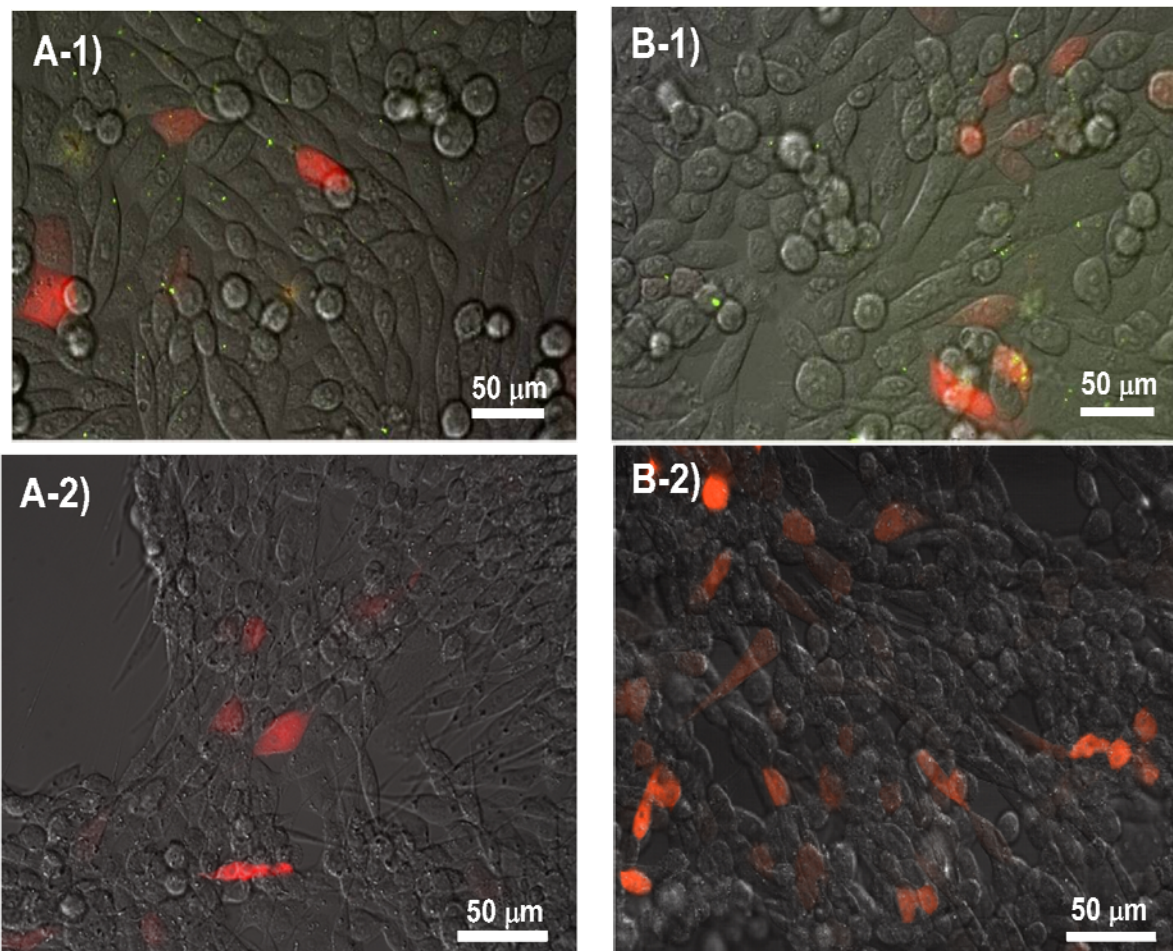
Figure 13: Wide field microscopy (10X) images of CHO cells transfected with (A) CdSe/ZnS-*S*-IDNA and (B) CdSe/ZnS-*NH*-IDNA using Optifect. Images taken at 24 h (A-1, B-1) and 48 h (A-2, B-2) post transfection. All images are taken immediately following media exchange.

While the QDs are observed to be localized within endosomes/lysosomes within the experimental timescales, DsRed-Express fluorescent protein is observed within the cytosol 24 h after transfection by the QD-IDNA package. Sustained expression is observed over the first 72 h and has been observed up to 96 h, at which point the cells reach confluency and are no longer tracked in our experiment. Since the QD is localized in the endosomal package and the appearance of DsRed-Express has a half life of ~ 24 h, the appearance of red photoluminescence in the cytosol implies that the gene and its promoter have rapidly disassembled from the QD surface.

Although no linker coupling dependence is observed for delivery of the QD-IDNA package, a clear coupling dependence is observed with respect to the level of expression of DsRed-Express. A higher level of protein expression for the cells transfected with QD-*S*-IDNA over the cells transfected with QD-*NH*-IDNA is observed for InP/ZnS in Figures 12. The images of cells transfected with CdSe/ZnS constructs, however, show a higher level of protein expression in cells transfected with QD-*NH*-IDNA over those transfected with QD-*S*-IDNA. The difference in the time dependent expression levels for coupling chemistries suggests that the strength of the QD-IDNA aggregate may be affected by the loading level of the DNA linker on the QD surface as well as the type of passivant layer on the QD.

To confirm the optical microscopy observation of protein expression levels, the time dependent expression levels for the fluorescent protein in the cell were statistically analyzed using flow-cytometry for >30,000 events (2X replicate) (Figure 14). A visual comparison of the protein expression levels measured by flow cytometry for 4 μg naked IDNA per 20 μL Optifect concentrations at 24 h, 48 h, and 72 h is shown in Figure 14. The levels of DsRed-Express expression for each of the samples are listed in Table 1. To eliminate false positives arising from excess material in the media, the media was exchanged prior to data collection. The negative control was used to set the positive threshold at 0.1 % of all events (A4 & B4).

Table 1: Flow cytometry results for DsRed-Express expression in CHO cells at 24, 48, and 72 h after transfection with InP/ZnS-*S*-IDNA, InP/ZnS-*NH*-IDNA, CdSe/ZnS-*S*-IDNA, and CdSe/ZnS-*NH*-IDNA.

	Naked IDNA	InP/ZnS		CdSe/ZnS	
		S	NH	S	NH
24 h	24.0 ± 2.4	10.6 ± 1	2.3 ± 0.35	6.0 ± 2.4	39.1 ± 10.2
48 h	38.8 ± 4.0	15.4 ± 0.85	2.3 ± 0.1	24 ± 9.1	58.4 ± 5.35
72 h	62.1 ± 6.0	39.3 ± 0.7	21.9 ± 3.55	8.8 ± 0.2	78.1 ± 10.4

The flow cytometry data indicates that at each time point both InP/ZnS-IDNA samples exhibit lower DsRed-Express expression levels than the naked IDNA sample.

Comparison of the expression levels between the InP/ZnS samples indicate the QD-*S*-IDNA yields faster expression (within 24 h) and a higher total expression rate within the experimental time scale than the QD-*NH*-IDNA. By 72 h the *S*-IDNA protein expression level is approaching the level of the naked IDNA; however the *NH*-IDNA sample is only showing marginal protein production at 72 h, although it is rising rapidly. Unfortunately looking at longer time points is difficult due to the cells reaching 100 % confluence, thus limiting the total experimental timescale for the experiment.

The flow cytometry data indicates a different pattern for DsRed-Express expression from CdSe/ZnS-IDNA samples. Similar to the InP/ZnS samples, the CdSe/ZnS-*S*-IDNA sample exhibits lower protein expression than the naked IDNA; however, the CdSe/ZnS-*NH*-IDNA sample exhibits a much higher expression level than the naked IDNA. Comparison of the expression levels between the CdSe/ZnS samples indicate the QD-*NH*-IDNA yields a faster expression (within 24 h) and a higher total expression rate within the experimental time scale than the QD-*S*-IDNA. This is trend is opposite from the InP/ZnS-IDNA samples described above. Although the QD-*NH*-IDNA follows the same expression rate as naked IDNA, the QD-*S*-IDNA sample drops off at 72 h.

The apparent difference in gene expression for *NH*-IDNA vs *S*-IDNA implies that delayed release from the QD is impacting the timing of expression. The higher level of DsRed-Express expression in the naked IDNA relative to three of the four QD-IDNA packages most likely reflects the faster endosomal release and protein expression of the naked IDNA as compared to the QD-IDNA package. The slow approach to the same level of expression reflects the timescale for DsRed-Express maturation, which is 33 h. The observations in Figures 12-14 strongly imply that chemoselective chemistries can be used to intentionally delay gene expression within a cell. Such an observation may have an important impact on use of QD-gene therapeutics where it is desirable to delay gene therapy response.
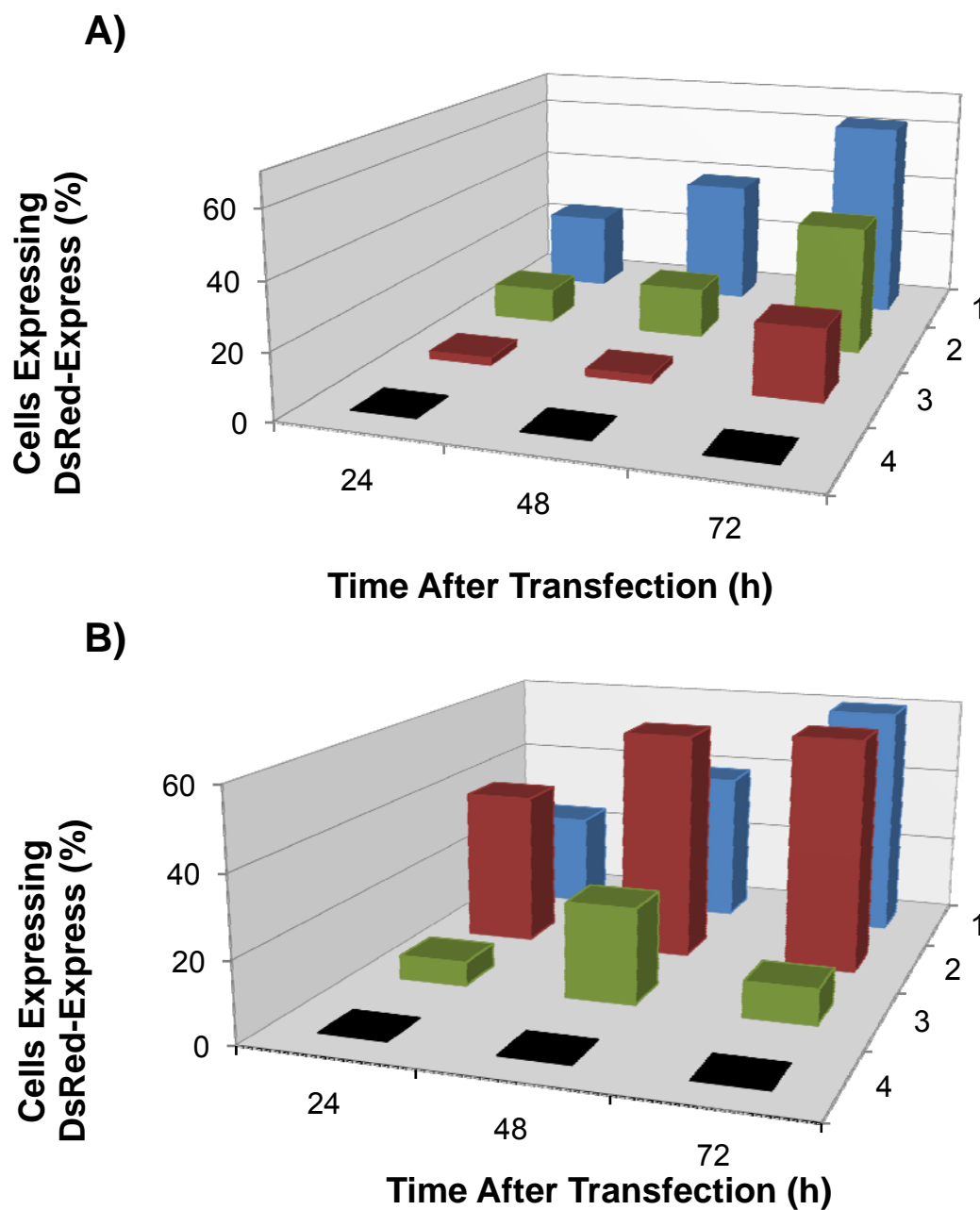
Figure 14. A) Flow cytometry data for CHO cells transfected with (A-1) naked lDNA, (A-2) InP/ZnS-*S*-lDNA, (A-3) InP/ZnS-*NH*-lDNA, and (A-4) negative control at 24 h, 48 h, and 72 h using Optifect. B) Flow cytometry data for CHO cells transfected with (B-1) naked lDNA, (B-2) CdSe/ZnS-*S*-lDNA, (B-3) CdSe-*NH*-lDNA, and (B-4) negative control at 24 h, 48 h, and 72 h using Optifect.

Conclusions

The observed level of DsRed-Express expression at any time point depends on the concentration of lDNA transfected, the rate of release of the lDNA from the QD-lDNA aggregate, and the rate of escape of the lDNA from the endosome. The optical data in Figure 10 indicates the concentration of DNA$_{linker}$ per QD varies depending on the type of coupling chemistry used. In the optical microscopy images in Figures 12-13, no QD is observed to be present out of the endosome, indicating release of the lDNA is the limiting step resulting in the apparent differences in expression levels. If we consider the fact that the release of the lDNA from the QD-lDNA aggregate is controlled by the number of Zn^{2+} interactions with the phosphate backbone of the lDNA, and the number of Zn^{2}+ ions available for interaction is affected by the number of DNA$_{linker}$ strands coupled to the surface[86-90]; then it is reasonable to assume the difference in expression levels for DsRed-Express must reflect the chemoselective chemistries of the underlying DNA$_{linker}$ to the QD surface.

Another plausible contribution to the degradation of the QD-lDNA aggregate is the glutathione (GSH) reduction of the QD-*S*-R bond of the DNA$_{linker}$ to the QD, which in turn disturbs the interaction between the phosphate backbone of the lDNA and the free Zn^{2+} ions. Earlier studies by Rotello and Wang have suggested this mechanism is most likely governed by glutathione uptake into the endosome resulting in reduction of the Au-thiol covalent coupling at the QD surface.[58,60-62] The level of GSH in all cases is expected to be the same; therefore it is reasonable to believe that the chemoselective chemistries affect the expression rate of DsRed-Express. In both cases, the link to the QD surface is identical, namely via a QD-*S*-R interaction. The only apparent significant difference is the length of the thiol spacer (RC$_6$ for *S*-DNA$_{linker}$ and C$_{11}$-C(O)NH-C$_6$ –R for the *NH*-DNA$_{linker}$), which would not be expected to have a significant impact on the reduction potential of the QD-*S*-R bond. Thus the observed difference in expression rate and levels must reflect the fact that the release rates and eventual expression levels are not dictated by the strength of thiol-surface atom bond and therefore it is likely a reflection of the site of appendage.

Considering the details of the chemoselective chemistries applied, the *S*-represents a thiol exchange reaction and will occur primarily at the most reactive site

(easiest exchange site) of a quantum dot, which is the vertices and edges of the material (Figure 8A & 8C). The *NH-* coupling chemistry is a condensation reaction between NH_2-lDNA and the acid (R-COOH) head group of the ligand passivating shell on the QD. The condensation reaction is expected to occur at the highest concentration of acid functionalities, which will be on the facets of the QD (Figure 8B & 8D). Since GSH mediated release controls the rate of DNA_{linker} escape from the QD surface, the *S*-lDNA release will be faster than the *NH*-DNA_{linker} since the initial exchange for *S*-DNA_{linker} is at a reactive exchange site. Such observations have been made for self assembled monolayers on gold and on metal nanoparticles.[91-92] In addition, further stabilization of the facet coupled site may arise from van der Waals interactions of the adjacent mercapto undecanoic acid chains on the facet of the QD surface, enhancing the delayed release for the *NH*-DNA_{linker}.

Although this work does not provide a complete mechanism for QD scaffolds in gene therapeutics, it does lay the foundation for chemoselective control over dosage within the cells. The purpose of forming an lDNA aggregate around the QD-DNA_{linker} construct was to create a basis from which to further refine chemoselective dosage control. This provided an understanding of the release rate from the surface of a QD in a cellular environment and how that can be controlled by differing passivant layers on the QD as well as the type of coupling chemistry used. This also highlighted the important electrostatic interactions between long strands of DNA and the QD surface. In effect, this work acts as the control experiment for a sophisticated drug delivery scaffold in which a desired gene can be covalently coupled to the surface of a QD in such a manner as to control its release within a cell. This may provide a promising breakthrough between QDs and gene therapeutics.

CHAPTER 4

USING CELL PENETRATING PEPTIDES FOR QUANTUM DOT UPTAKE

This chapter investigates the use of the widely used cell penetrating peptide (CPP), GRKKRRQRRRPPQ, derived from the HIV-1 transactivating factor (TAT),[66] to passivate the surface of 3.5 nm InP/ZnS and CdSe/ZnS core-shell QDs and monitor the effects on cellular uptake and metabolic toxicity in varying cell types.   The cell penetrating QDs were prepared through surface ligand exchange with either 90 % of the peptide CAAKA plus 10 % of the positively charged peptide CAAKA-TAT or 100 % of CAAKA-TAT (Figure 15).   Tracking of the cellular uptake of these QDs by optical microscopy shows rapid, diffuse accumulation of both the 10 % TAT and 100 % TAT passivated QDs throughout the cytosol of the cells. Toxicity studies were conducted by flow cytometry to investigate the effects of these materials on apoptosis, necrosis, and metabolic damage in Chinese Hamster Ovary (CHO) cells. These studies suggest toxic effects of the cell penetrating QDs are dependent on the amount of CAAKA-TAT used on the surface of the QD as well as the concentration of QD added.   These observations aid in the use of QDs as self transfecting, nano delivery scaffolds for drug or gene therapy.
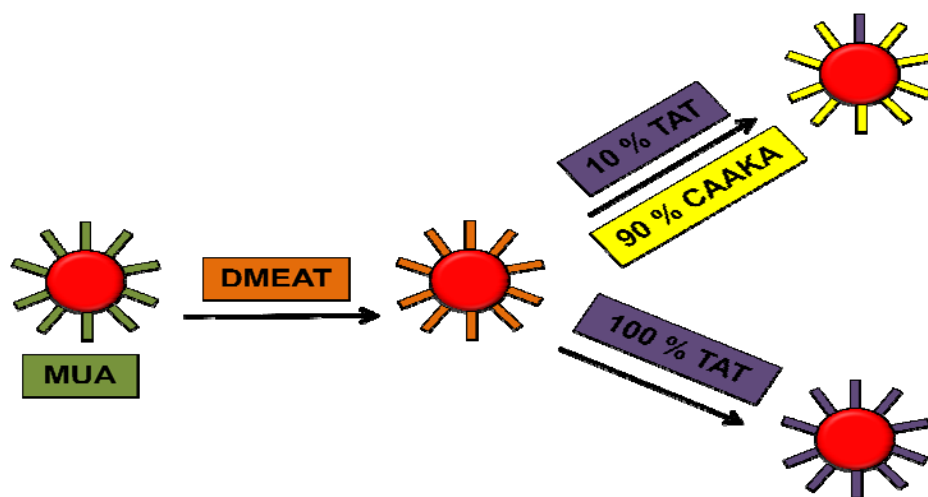
Figure 15: Schematic showing synthesis of QDs co-passivated by 10 % CAAKA-TAT and 90 % CAAKA as well as QDs passivated by 100 % CAAKA-TAT.

Materials and Methods

      CAAKA-TAT passivated QDs Method One. InP/ZnS and CdSe/ZnS QDs were passivated by CAAKA-TAT in two steps. First, dimethylaminoethanethiol (DMAET) was added to hexadecylamine (HDA) capped QDs in a 60:40 solution of toluene:DMF until an even suspension was reached. Small amounts of DMF were added to break up aggregates and obtain an even suspension. The QD solution was washed with DMF two times by removing the DMF supernatant after centrifugation and resuspending the pellet in fresh DMF. After the final wash, the QD-DMAET pellet was resuspended in potassium phosphate buffer (50 mM, pH 7.2) with vortexing and sonication. The QDs were then precipitated with ethanol to remove unwanted organic contaminants and solubilized in potassium phosphate buffer. The peptides (CAAKA and CAAKAGRKKRRQRRRPPQ) were added to the QD-DMEAT solution in the desired ratio (90:10 or 0:100) and allowed to sit overnight to allow for ligand exchange. The QDs were cleaned up and purified as described for the first ligand exchange step.

      CAAKA-TAT passivated QDs Method Two. MUA passivated quantum dots were dissolved in a 9:1 Pyridine: DMF solution under inert conditions. A stock solution of peptides (1mg/100 μL), dissolved in nanopure H_2O, was injected to the nanoparticle solution. Tetramethylammonium hydroxide (300 μL) was injected and left to stir for 1.5 hrs in the dark. The aqueous portion of the resulting bi-phasic solution was collected and centrifuged. The pellet was resuspended in DMF and centrifuged twice to remove any Pyridine that might have been present. Lastly, the pellet was resuspended in nanopure H_2O. Additional peptide was added if necessary to help solubility.

      Cell Transfection by CPP-QDs. The MUA passivated InP/ZnS and DHLA passivated CdSe/ZnS (10 nM) QDs were transfected into Chinese Hamster Ovary (CHO) cells at 30 % confluence (~0.5 x 10^6 cells) in a 35 mm live-cell imaging dish (Matteck Corp) using the transfecting cationic lipid Optifect according to manufacturer's protocols (Invitrogen). The varying CPP passivated QDs were transfected into CHO cells at 30 % confluence (~0.5 x 10^6 cells) in a 35 mm live-cell imaging dish (Matteck Corp) by incubating the cells with premixed CPP-QDs and cell media at 37 °C. CHO cells were grown at 37 °C in Dulbeccos Modified Eagle's Medium (DMEM, Gibco)

supplemented with 10 % non-essential amino acids, 10 % cosmic calf serum, 1 % antibiotics / antimycotics, and 0.1 % Gentamycin.

Optical detection of CPP-QDs cellular uptake. Confocal images of the cells were taken on a Nikon T2000E C1SI spectral confocal microscope to analyze the internalization and localization of the varying QDs. Epifluorescent images were taken of the cells at multiple time points after transfection to monitor the level of uptake of CPP-QDs.

Viability Assays. The impact of MUA-InP/ZnS, TAT-InP/ZnS (100 %), DHLA-CdSe/ZnS, and TAT-CdSe/ZnS (100 %) on the percentage of apoptotic and dead cells in a given CHO cell culture was assessed using the Vibrant Apoptosis Assay Kit #2 (Invitrogen, V13241). The impact of InP/ZnS with varying amounts of CAAKATAT on the viability and metabolic efficiency of CHO cells was assessed using the Live/Dead Cell Vitality Assay Kit (Invitrogen, L34951). The cells were incubated with QDs for 24 h and stained according to manufacturer's protocol for each type of assay. The stained cells were analyzed by flow cytometry (10,000 events). The flow cytometry was accomplished on a BD FACS Canto II with 488 nm excitation and detection on FITC (530/15) and PE-A (585/42) filter sets.

Results and Discussion

CPP-QD Synthesis and Characterization. The 3.5 nm InP/ZnS and CdSe/ZnS QDs were modified with the peptides CAAKA and CAAKATAT to promote water solubility and cellular uptake. The CAAKA peptide is neutral and acts as a controlled place-holder on the surface of the QDs. The TAT peptide has a slightly positive charge allowing it to penetrate cellular membranes. The CAAKA sequence was added to the base TAT sequence to allow for consistency at the surface of the QDs. As seen in Figure 15, the peptide passivant layers were accomplished through simple ligand exchange reactions. Water soluble MUA passivated QDs were used as a control against which the CPP-QDs could be examined.
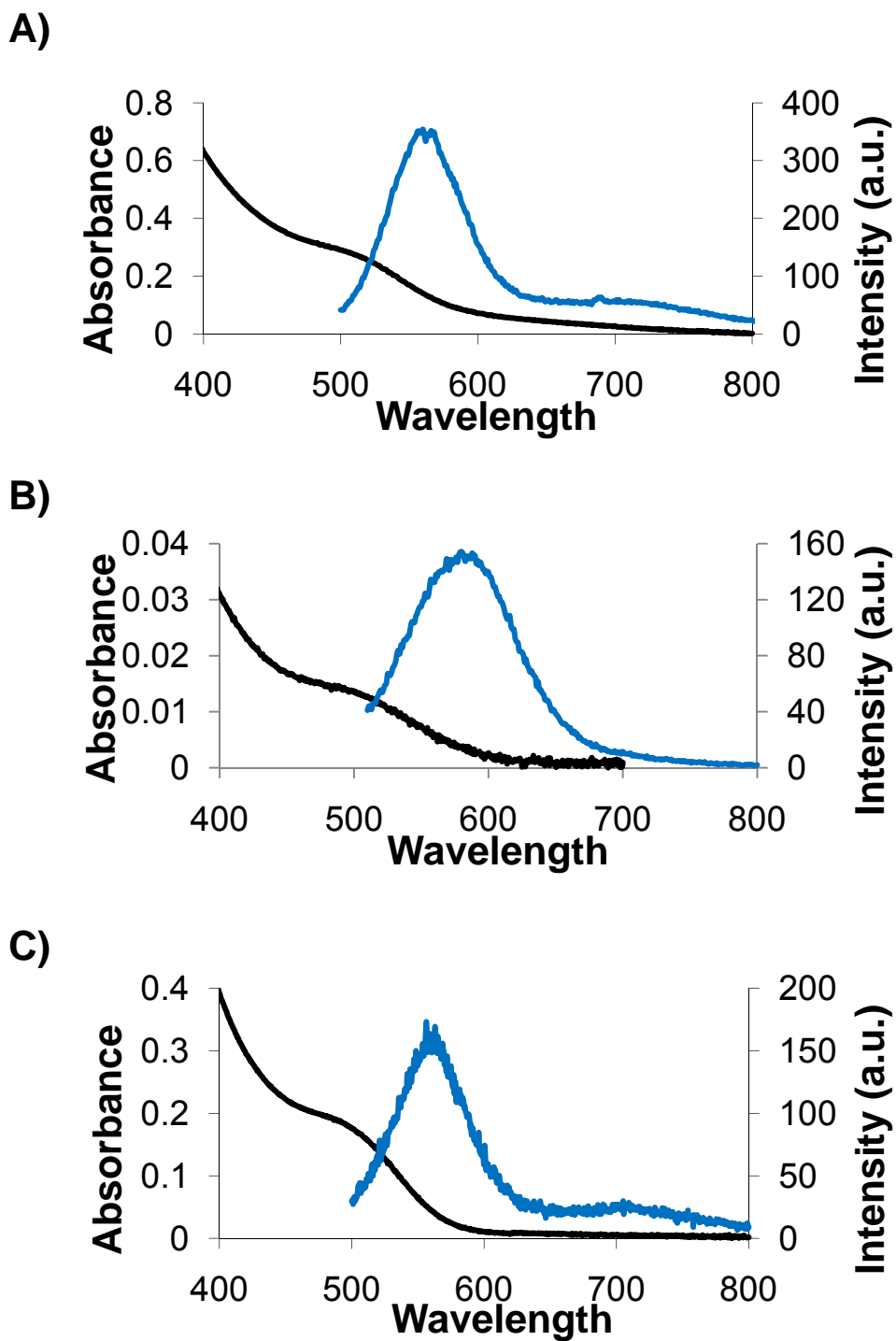
Figure 16: Absorbance and emission of 3.5 nm InP/ZnS A) passivated by MUA in KPB, B) co-passivated by 90 % CAAKA and 10 % CAAKATAT in KPB and C) passivated by 100 % CAAKATAT in KPB.

Characterization of these QD modifications was performed by optical absorption and photoluminescence analysis (Figure 16) to determine changes in water solubility and emission intensity. The absorbance and photoluminescence of MUA-InP/ZnS are shown in Figure 16A. The absorbance and photoluminescence of TAT-InP/ZnS co-passivated by 90 % CAAKA and 10 % CAAKATAT are shown in Figure 16B. This sample was made using method 2 described above. The absorbance and photoluminescence of TAT-InP/ZnS passivated by 100 % CAAKATAT are shown in Figure 16C. This sample was made using method 1 described above. All samples were excited at 460 nm for emission analysis. At first glance, it appears that increased TAT on the surface decreases the emission intensity of the InP/ZnS. However, using the absorbance to correct for concentration shows the emission intensities for MUA-InP/ZnS and TAT-InP/ZnS (100 %) are essentially equivalent. The emission intensity for TAT-InP/ZnS (10 %) is an order of magnitude higher than either of the other samples. This suggests a greater surface passivation, or tighter packing of surface ligands, by the 10 % TAT than the 100 % TAT or MUA.

CPP-QD Transfection and Uptake into CHO Cells. The MUA-QDs and TAT-QDs were transfected into CHO cells and monitored for uptake and toxicity affects by fluorescece microscopy. The MUA-QDs were transfected with the cationic lipid Optifect while the TAT-QDs were transfected through endosomal uptake resulting from the interactions of the positively charged peptide with the negatively charged cellular surface. Cationic liposomes are known to create micellar-like structures and carry their contents into large endosomes ranging from 30 – 250 nm.[79] At 24 h post transfection, the internalized MUA-InP/ZnS QDs are located in 2-3 μm endosomes, as seen in Figure 17A. TAT is also known to internalize through endosomal mechanisms, but the resulting endosomes are much smaller.[66] At 24 h post transfection, the TAT-InP/ZnS (10 %) QDs are punctate (Figure 17B) isolated in smaller aggregates (< 1 μm) associated with the exterior cellular membrane and internalized in endosomes throughout the cell. To provide unequivocal evidence of QD internalization, the cellular membranes were stained with Alexa Fluor 594 wheat germ agglutinin (red) and the nuclei were stained with Hoescht 34580 (blue). Additionally, confocal z-stack images were taken for each type of transfection, providing a three dimensional view. A 3-D

stack of the MUA-QDs (Figure 17A-2) clearly shows the QDs (yellow) within the cellular membrane. The z-stack images for TAT-QDs are shown in tile format in Figure 17B-2. It is clear that the majority of the QDs appear as punctate in the same focal plane as the nucleus, indicating the QDs are internalized in endosomal vesicles within the cells, and more importantly appear to be localizing at the perinuclear membrane.
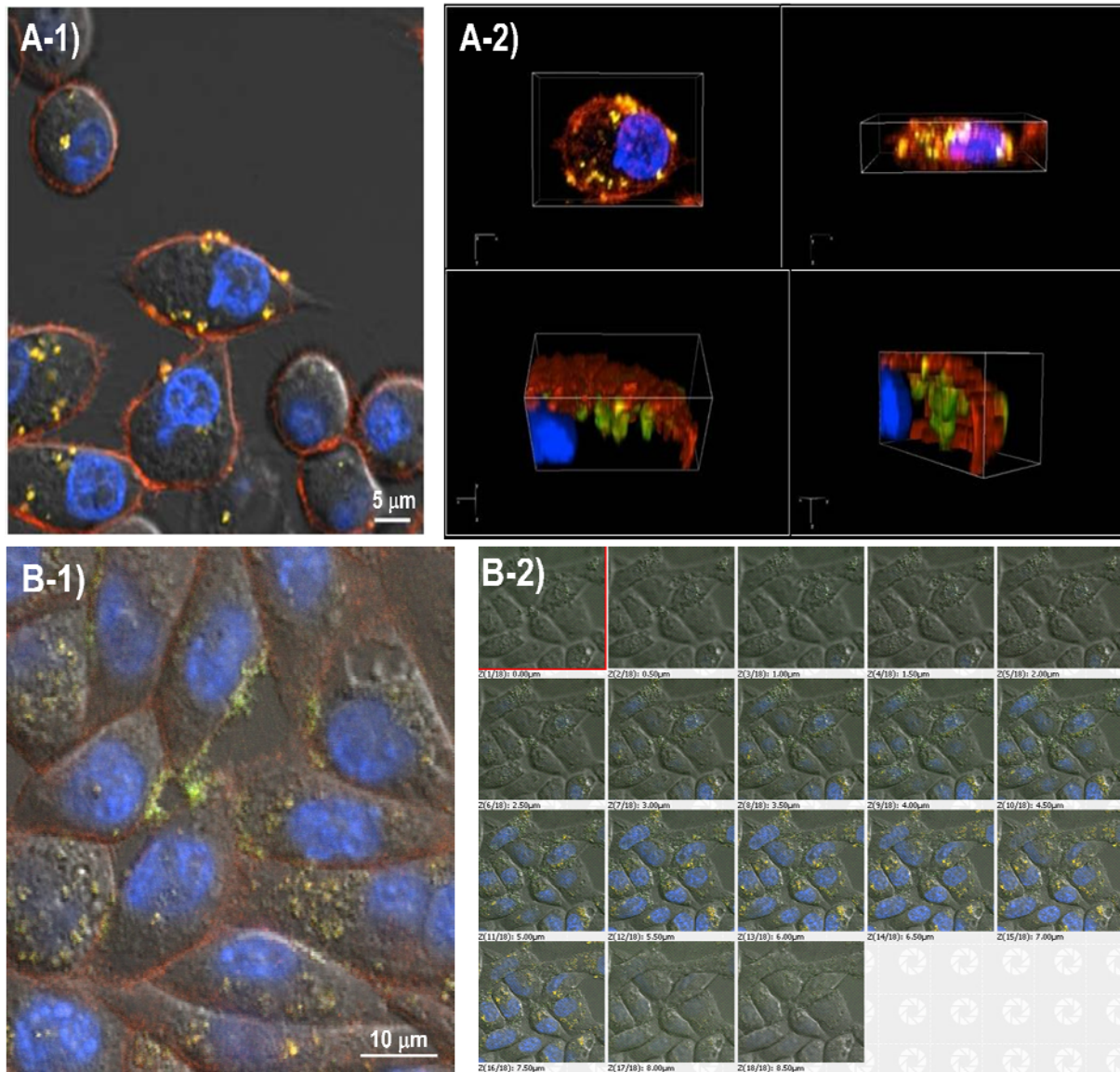
Figure 17: Confocal microscopy images of A) CHO cells transfected with InP/ZnS-MUA and B) CHO cells transfected with InP/ZnS-TAT (10 %). A-1 and B-1 are single plane 40X images. A-2 and B-2 are representative z-stack images. The cell nuclei are stained with Hoescht 34580. The cell membranes are stained with Alexafluor 594 wheat germ agglutinin.

CPP-QDs Transfection and Uptake into HMSC and LNCaP Cells. The CPP-QDs were transfected into other cell types to monitor the universal uptake characteristics of the TAT peptide. Confocal microscopy images in Figure 18A show Human Mesenchymal Stem Cells (HMSC) 24 h post transfection with TAT-CdSe/ZnS (10 %). The images show punctate localization of the InP/ZnS within endosomal vesicles. The z-stack images in Figure 18A-2 show the Hoescht 34580 stained nucleus (blue) in the same focal plane as the QDs (green), providing evidence for QD internalization in analogy with the CHO cells. The confocal microscopy images in Figure 18B show Green Fluorescent Protein (GFP) expressing human prostate cancer (LNCaP) cells 24 h post transfection with TAT-CdSe/ZnS (10 %). The QDs are internalized into similar sized endosomes as in the HMSC and CHO cells. The z-stack 3-D images in Figure 18B-2 show the QDs (red) in the midst of the GFP (green) emitting cell, providing evidence for QD internalization.
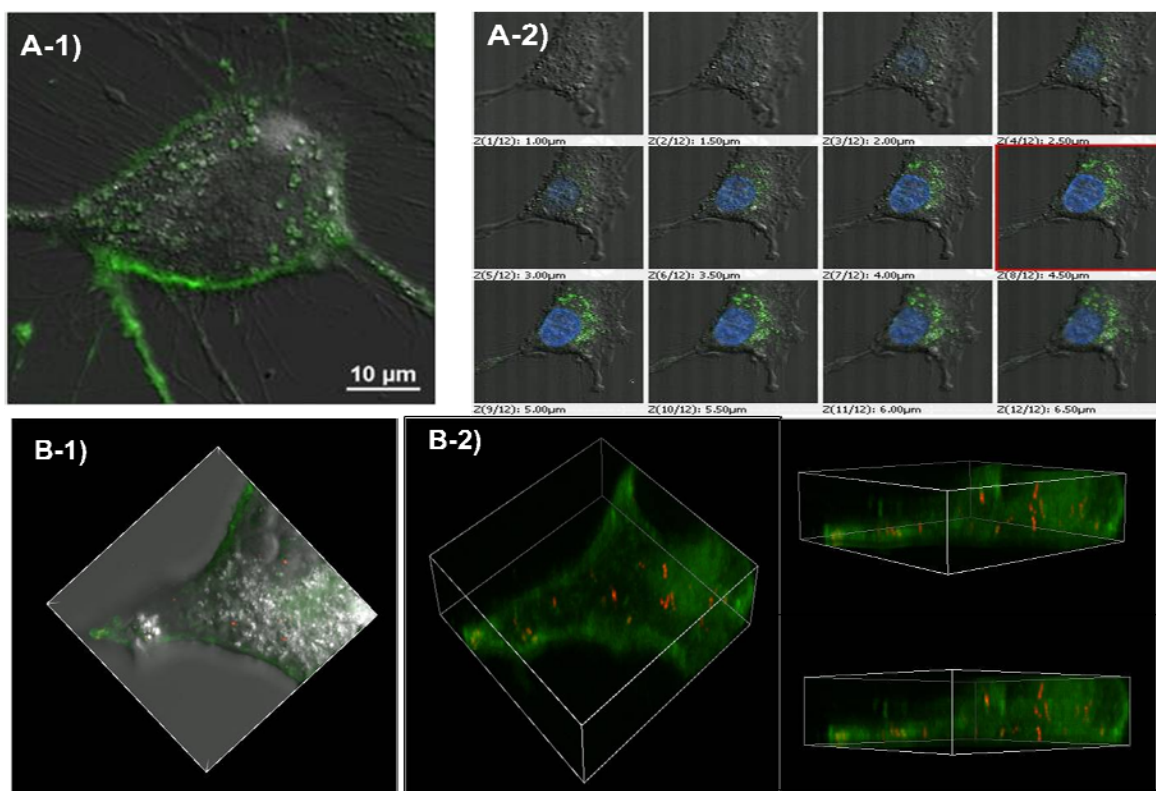
Figure 18: Confocal microscopy images of A) HMSC cells transfected with CdSe/ZnS-TAT (10 %), and B) LNCaP-GFP cells transfected with CdSe/ZnS-TAT (10 %). A-1 and B-1 are single plane 40X images. A-2 and B-2 are representative z-stack images. The nucleus in A-2 is stained with Hoescht 34580.

Time Dependent Uptake. A comparison of the uptake of TAT-InP/ZnS (10 %) and TAT-InP/ZnS (100 %) was accomplished through time-dependent epifluorescent microscopy images of the transfected CHO cells (Figure 19). At 1 h post transfection, the TAT-InP/ZnS (10 %) QDs are seen in small aggregates throughout the cell media that are beginning to associate with the cellular membrane (Figure 19A-1). By 24 h post transfection, the QDs are clearly seen within the cytosol of the cells with some perinuclear localization (Figure 19A-2). The CHO cells in this case appear to remain healthy, maintaining contact with the dish. At 2.5 h post transfection, the TAT-InP/ZnS (100 %) QDs are seen in large aggregates throughout the cell media and associated with the cellular membrane of the CHO cells (Figure 19B-1). The cells appear to be detached from the surface of the dish, indicating cellular disturbance by the QDs. By 24 h post transfection, the cells have not reattached, as is common with the Optifect transfections, and they appear to be completely filled with the QDs (Figure 19B-2).
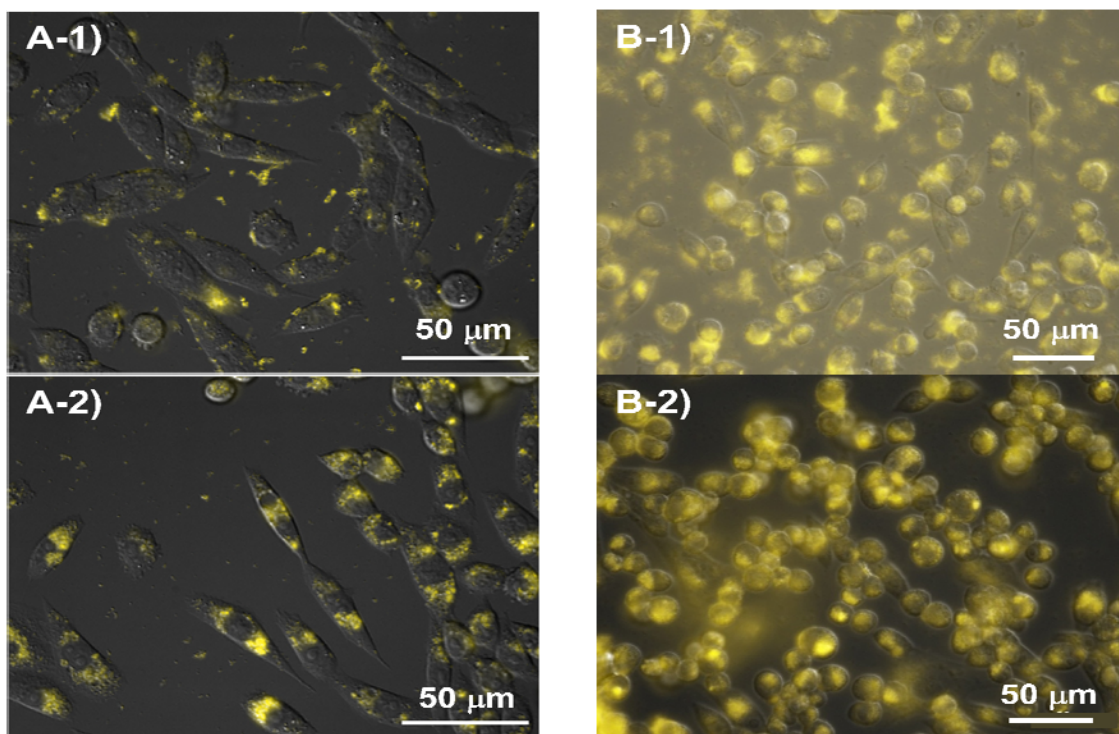
Figure 19: Epifluorescent microscopy images (40X) of CHO cells transfected with InP/ZnS (A) co-passivated by 90 % CAAKA and 10 % CAAKATAT and (B) passivated by 100 % CAAKATAT. Images were taken post transfection at (A-1) 1 h, (A-2) 24 h, (B-1) 2.5 h, and (B-2) 16 h.

Viability Assays. The uptake of the QDs can impact cellular function or initiate an apoptotic response due to cellular oxidative stress. Evidence of cellular disturbance is seen in Figure 19B and combined with a lack of cell proliferation after 24 h, indicates that the 100 % CAAKATAT QD samples may hinder cellular growth. To confirm the optical microscopy observations and determine the mechanism through which cell proliferation is hindered, transfected cells were statistically analyzed by flow cytometry for 10,000 events using multiple fluorescent vitality and viability assays.

Vibrant Apoptosis Assay. The first assay, Vibrant Apoptosis Assay Kit #2 (Invtrogen), looked for an increase in apoptotic and dead cells 24 h after transfection. The cells were transfected with 10 nM MUA-InP/ZnS, TAT-InP/ZnS (100 %), DHLA-CdSe/ZnS, and TAT-CdSe/ZnS (100 %) and compared to a control sample of CHO cells. The reagents supplied in the kit include red-fluorescent propidium iodide (PI) and a recombinant Annexin V phospholipid-binding protein conjugated to green-fluorescent Alexa Fluor 488 (AF488) dye. Propidium iodide is a membrane impermeant, intercalating nucleic acid dye.[93-94] The annexin V conjugate has a high affinity for phosphatidylserine, which is translocated to the outer plasma membrane in apoptotic cells. [95-98] This combination allows for distinction between Live cells (no staining), apoptotic cells (green), and dead cells (red & green). A visual representation of the affects of each QD sample on CHO cells is shown in Figure 20, while Table 2 provides the average percentage of cells in each category.

Table 2: Flow cytometry results for CHO cells treated with InP/ZnS-MUA, InP/ZnS-TAT, CdSe/ZnS-DHLA, and CdSe/ZnS-TAT and stained after 24 h with PI and an annexin V AF488 conjugate. Values show what percentage of the total events were determined to be living cells, dead cells, and apoptotic cells.

	Control	InP/ZnS		CdSe/ZnS	
		MUA	**TAT**	**MUA**	**TAT**
Live	87.3 ± 2.6	86.1 ± 0.5	86.0 ± 4.8	82.7 ± 0.1	83.0 ± 1.1
Dead	10.7 ± 1.7	11.6 ± 0.7	11.6 ± 4.3	14.6 ± 0.4	14.8 ± 1.1
Apoptotic	2.0 ± 0.8	1.5 ± 0.2	2.1 ± 0.1	2.7 ± 0.3	2.2 ± 0.1

The flow cytometry data indicates no significant difference between the viability in the CHO cells exposed to MUA-InP/ZnS, TAT-InP/ZnS (100 %), DHLA-CdSe/ZnS, or TAT-CdSe/ZnS (100 %). There is a slight increase in dead cells when treated with CdSe/ZnS over the control and InP/ZnS may be statistical variance, although CdSe/ZnS has been suggested to have toxic effects on cells.[68,99] The cells treated with TAT-QDs show the greatest variability between samples in the living and dead cell categories. This may suggest that TAT disturbs the cellular membrane, allowing PI to enter, without fully killing the cells. This would create a population of partially stained cells which adds to the variability between the two distinct populations.
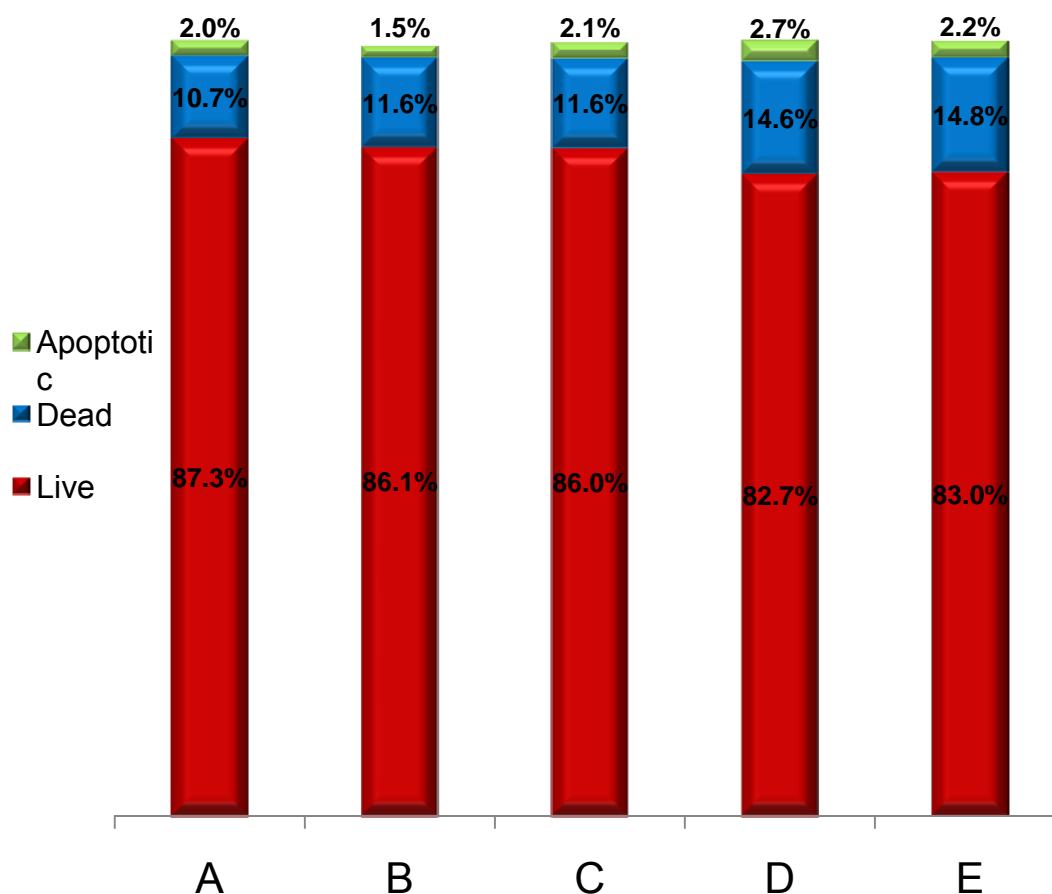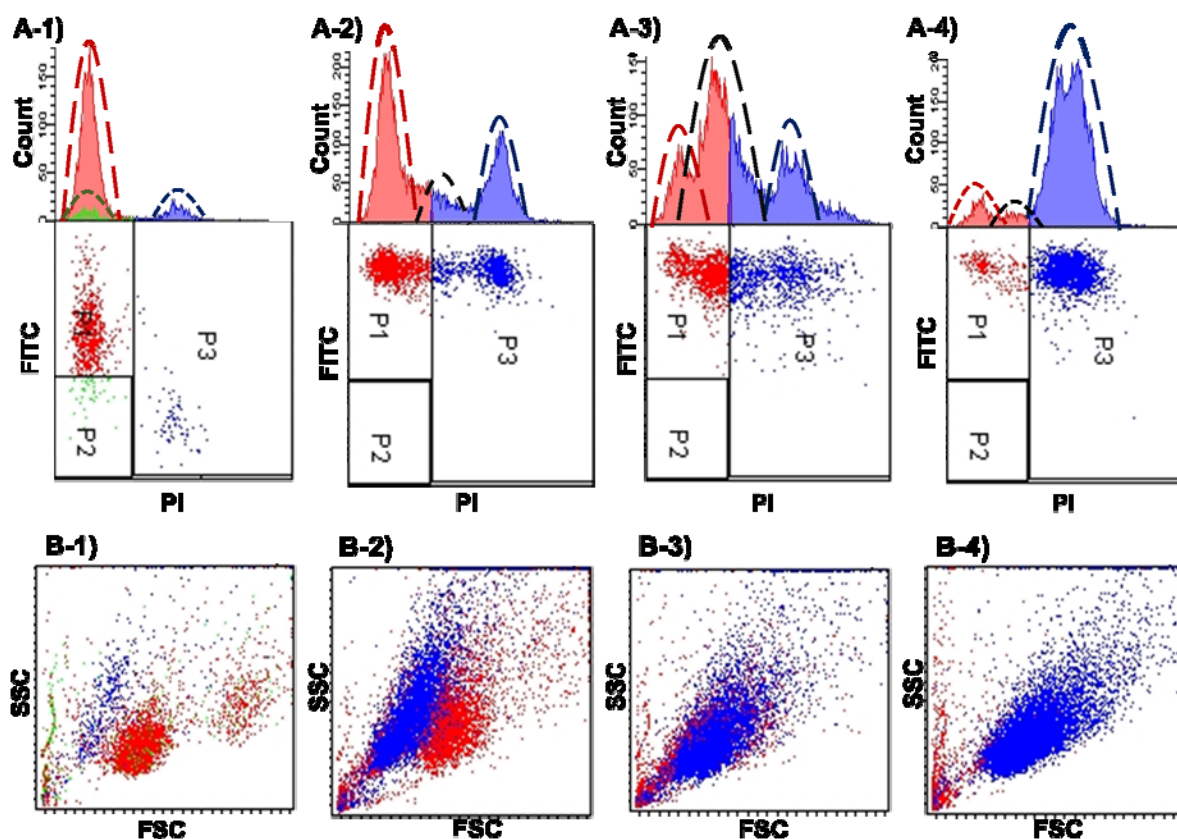

Figure 20: Flow Cytometry viability assay on CHO cells stained with Invitrogen Apoptosis/Necrosis Kit #2. Prior to staining the cells were A) grown normally (control), B) transfected with 10 nM InP/ZnS-MUA for 24 h, C) transfected with 10 nM InP/ZnS-TAT (100%) for 24 h, D) transfected with 10 nM CdSe/ZnS-DHLA for 24 h, and E) transfected with 10 nM CdSe/ZnS-TAT (100%) for 24 h.

Propidium Iodide Staining for Membrane Viability. In order to further investigate the possibility that TAT-QDs disturb the cellular membrane of CHO cells, PI staining was analyzed on CHO cells transfected with 5 nM, 10 nM, and 15 nM TAT-InP/ZnS (100 %) QDs. The raw flow cytometry data is shown in Figure 21. The graphs in Figure 21A show the different intensities of PI staining in the given CHO cell population. The cells in P1 (dashed red) are unstained and healthy. Cells in P2 (dashed green) are apopototic and stained with an Annexin V AF488 conjugate.[100] This stain was only used in the control sample. Cells in P3 (dashed blue) are fully stained with propidium iodide (PI) due to a compromised membrane. There is a clear shift in the populations from unstained, healthy cells (red) to PI stained cells (blue) as the concentration of QD increases (Figure 21 A-2→A-4). Cells between P1 & P3 (dashed black) are stained with propidium iodide, but with less intensity than the cells in P3. This indicates that these cells have a partially compromised membrane that allows for internalization of the PI stain, but not to the same extent as dead cells. The partially stained (dashed black) population is greatest at 10 nM and disappears at 15 nM. This shift indicates that the TAT-QDs disturb the membrane of the cells and eventually overwhelm it at increased concentrations.

The flow cytometry data in Figure 21B shows the comparison of side scatter (indicating cell granularity) and front scatter (indicating cell size). A shift in cellular granularity is also present as the concentration of TAT-QDs increases (Figure 21 B-2→B-4). The blue population in Figure 21B-1 represents the normal size/granularity distribution of dead cells (stained with PI) in a control population of CHO cells.[100] The granularity shift of the blue population (stained with PI) in the subsequent graphs indicates that the TAT-QDs are not causing cellular death, but most likely swelling the cells as they overwhelm the membrane. This data corresponds with the microscope images in Figure 19 where the CHO cells appear disturbed by the TAT-QDs (100 %) and are unable to attach to the dish surface. It also explains why the cells seem to go into a lag phase after transfection by the TAT-QDs (100 %). It can be suggested from the data above that the TAT-QDs (100 %) appear to result in metabolic damage to the CHO cells as the concentration increases. This would explain the hindered cell growth after transfection and the inability of the CHO cells to reattach to the surface of the dish.

Figure 21: Flow cytometry viability assay on CHO cells using Invitrogen Apoptosis/Necrosis Kit #2. The graphs show A) the number of events corresponding to the intensity of PI staining (x-axis) and B) the comparison of forward and side scatter created by the size and granularity of the cells. Prior to staining, the cells were A) grown normally (control), B) incubatedd with 5 nM TAT-InP/ZnS (100%) for 24 h, C) incubated with 10 nM TAT-InP/ZnS (100 %) for 24 h, and D) incubated with 15 nM TAT-InP/ZnS (100 %) for 24 h. Only the control cells (A) were stained with Annexin V AF488. The dashed lines are not fitted to the data and are for visual aid only.

Evidence of Oxidative Stress. Another flow cytometry vitality assay, the Live/Dead Cell Vitality Kit (Invitrogen), was chosen to distinguish the metabolically damaged cells from the healthy and dead cells. This kit identifies the metabolically active cells by their ability to reduce C_{12}-resazurin to red-fluorescent C_{12}-resorufin. It is believed that mitochondrial enzymes used in the cellular respiration process of healthy cells reduce the compound.[101-102] The dead cells are identified by the cell-impermeant, green-fluorescent nucleic acid stain, SYTOX green. This dye works similarly to PI in that it can only enter cells with compromised membranes and has a >500-fold

fluorescence increase upon binding with nucleic acids. With this combination, the healthy cells emit bright red fluorescence, the dead cells emit green fluorescence, and the metabolically damaged cells emit partially green and partially red fluorescence.

The Live/Dead cell vitality kit was used to look at differences in QD concentration as well as levels of TAT loading. The CHO cells were incubated with 5 nM, 10 nM, and 15 nM concentrations of TAT-InP/ZnS (10 %) and   TAT-InP/ZnS (100 %) for 24 h. The treated CHO cells as well as a control were stained with the appropriate reagents and statistically analyzed by flow cytometry (10,000 events). Each transfection was only done once for this assay. Visual representations of the affects of the QDs on the CHO cells are shown in Figure 22. The percentages shown are the percentage of cells in each category out of the total 10,000 events recorded by flow cytometry.

A comparison of the affects of increasing the QD concentration on cellular metabolism is shown in Figure 22A for the TAT-InP/ZnS (10 %) QDs and Figure 22B for the TAT-InP/ZnS (100 %) QDs. Figure 22 C-D emphasizes the affects of varying the TAT loading levels on the QDs. In both cases there is a decrease in living cells as the QD concentration increases as well as a corresponding increase in damaged or dead cells. The TAT-InP/ZnS (10 %) causes a greater increase in damaged cells while the TAT-InP/ZnS (100 %) causes a greater increase in dead cells. In fact, the TAT-InP/ZnS (10 %) follows a predictable pattern as the QD concentration increases, but the TAT-InP/Zns (100 %) seems to overwhelm the cells at 10 nM, leaving mostly dead cells and no living cells in the population. This seems to contradict the data in Figure 20, however it is important to note that comparisons cannot be drawn between the staining kits due to the different mechanisms of staining as well as the difference in dye intensities. Table 3 gives the percent difference between each sample and the control sample for each of the categories (dead, damaged, and live).

Table 3: Flow Cytometry results depicting affects of incubating CHO cells with increasing concentrations of TAT-InP/ZnS (10 %) and TAT-InP/ZnS (100 %). Percentages indicate the percent difference between the number of CHO cells in each category in the control sample and the number of CHO cells in each category after incubation with each sample. The arrows depict either an increase (↑) or a decrease (↓) over the control sample.

	Damaged		Dead		Live	
	10 % TAT	**100 % TAT**	**10 % TAT**	**100 % TAT**	**10 % TAT**	**100 % TAT**
5 nM	63.8 % ↑	3.19 % ↑	94.9 % ↑	110 % ↑	60.5 % ↓	57.6 % ↓
10 nM	216 % ↑	108 % ↑	80.8% ↑	152 % ↑	75.6 % ↓	101 % ↓
15 nM	363 % ↑	124 % ↑	57.7 % ↑	151 % ↑	88.2 % ↓	101 % ↓
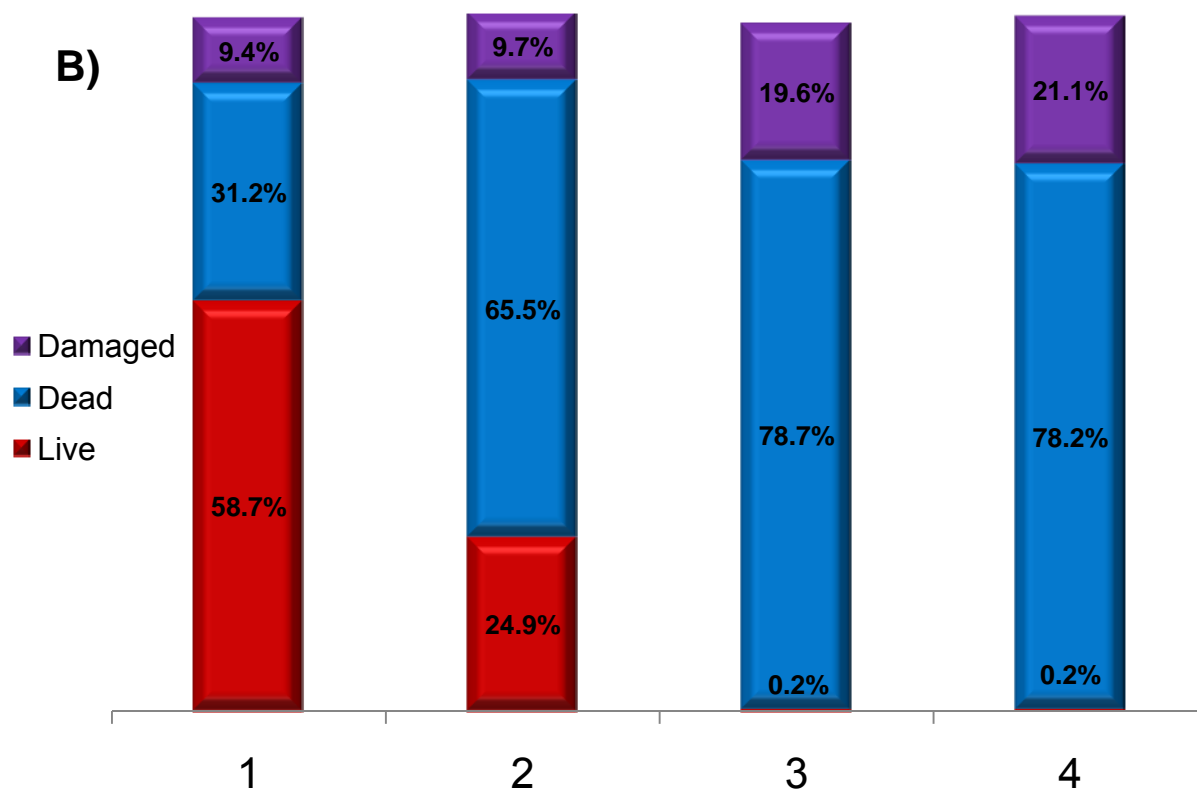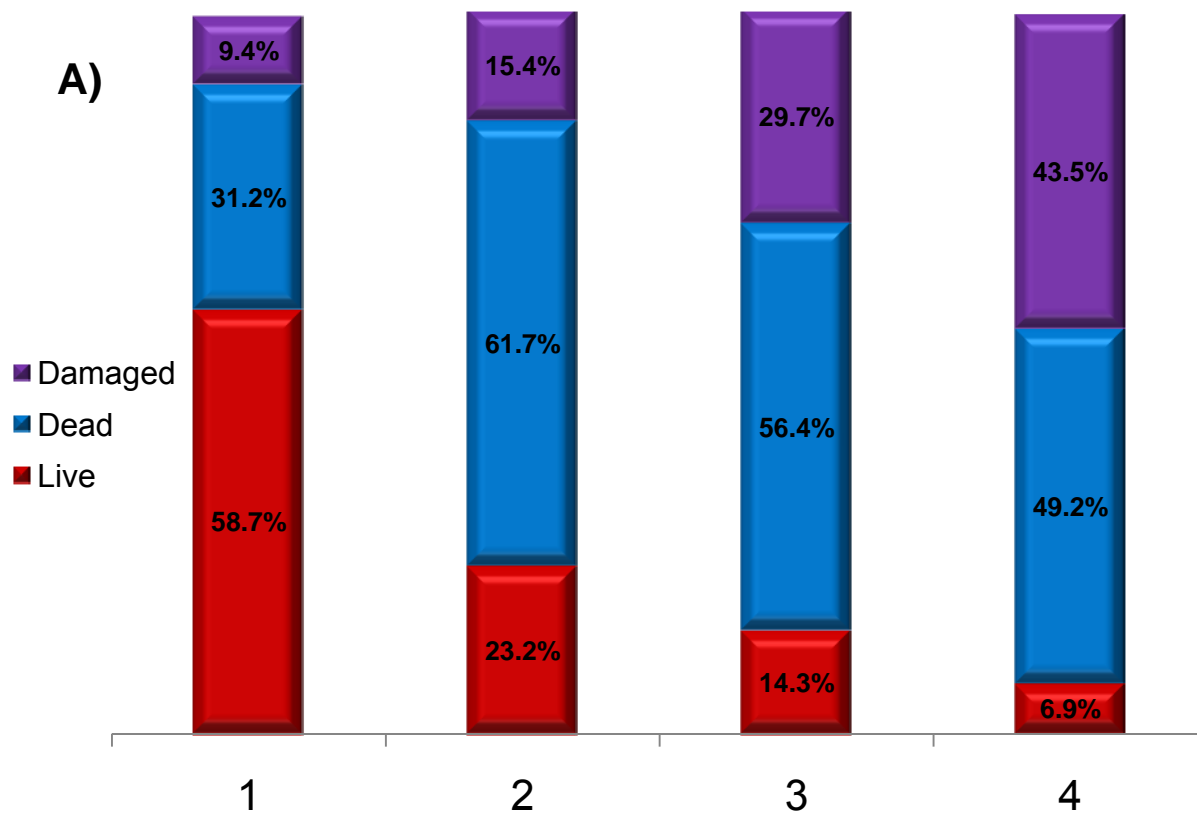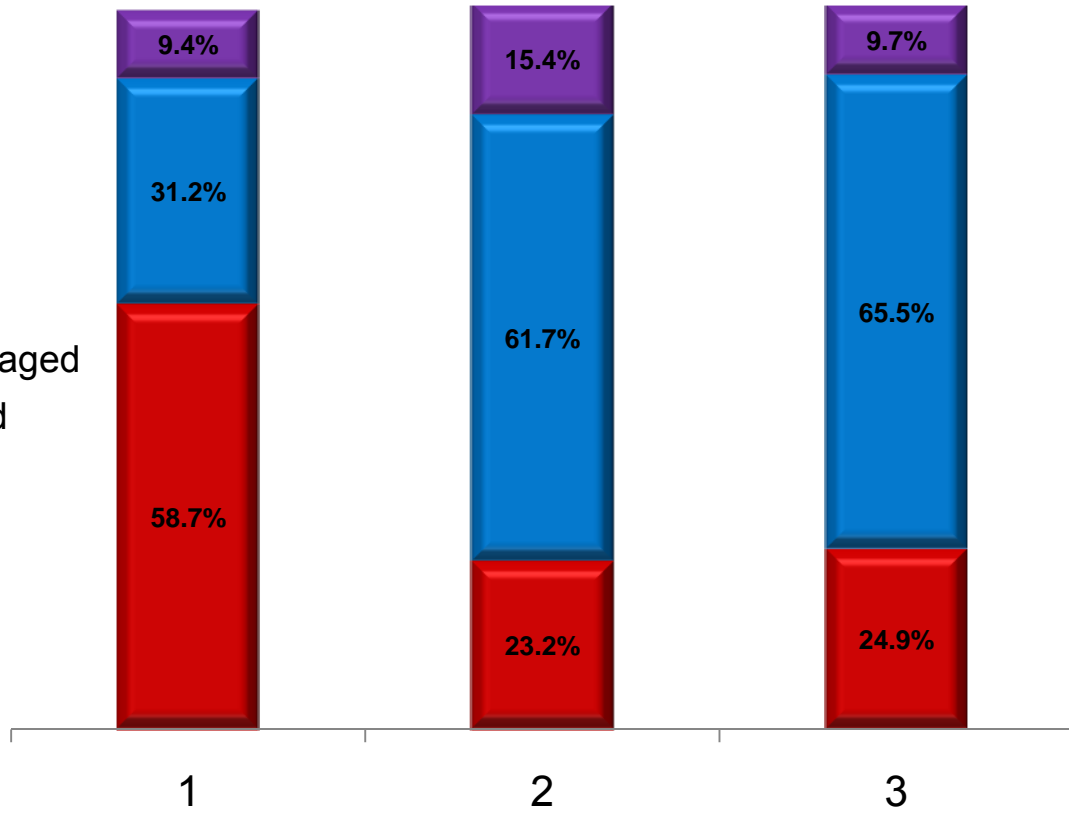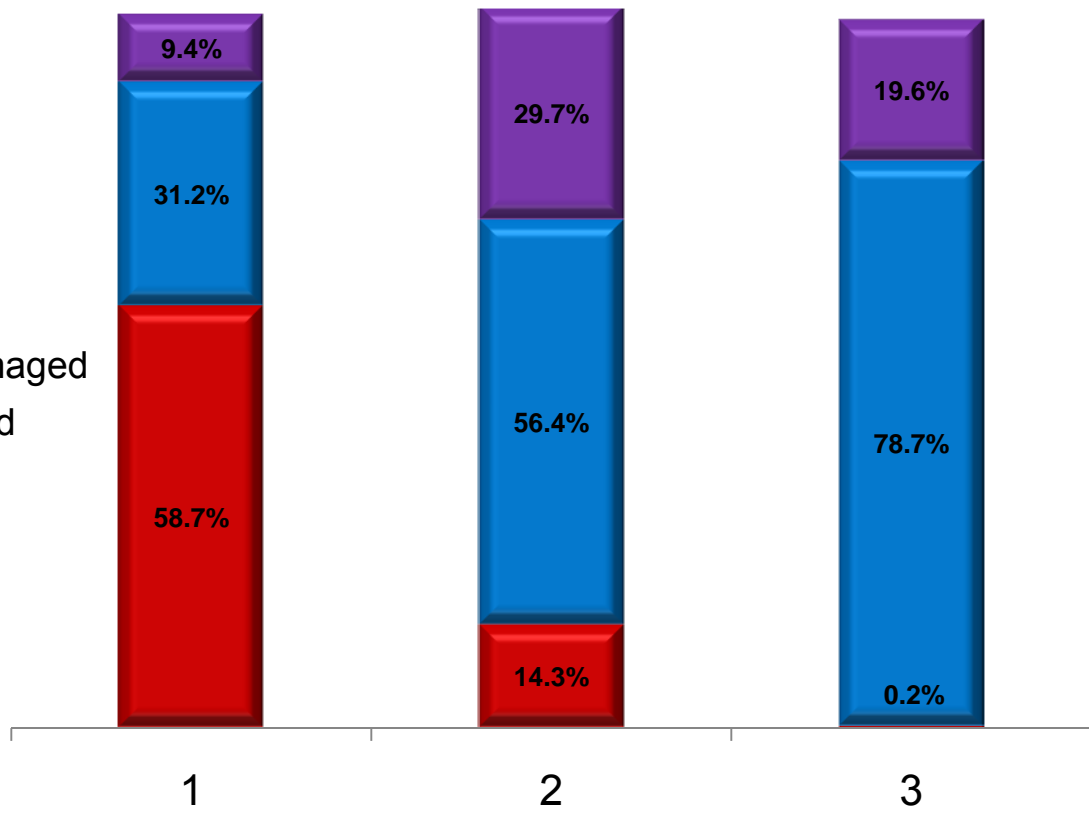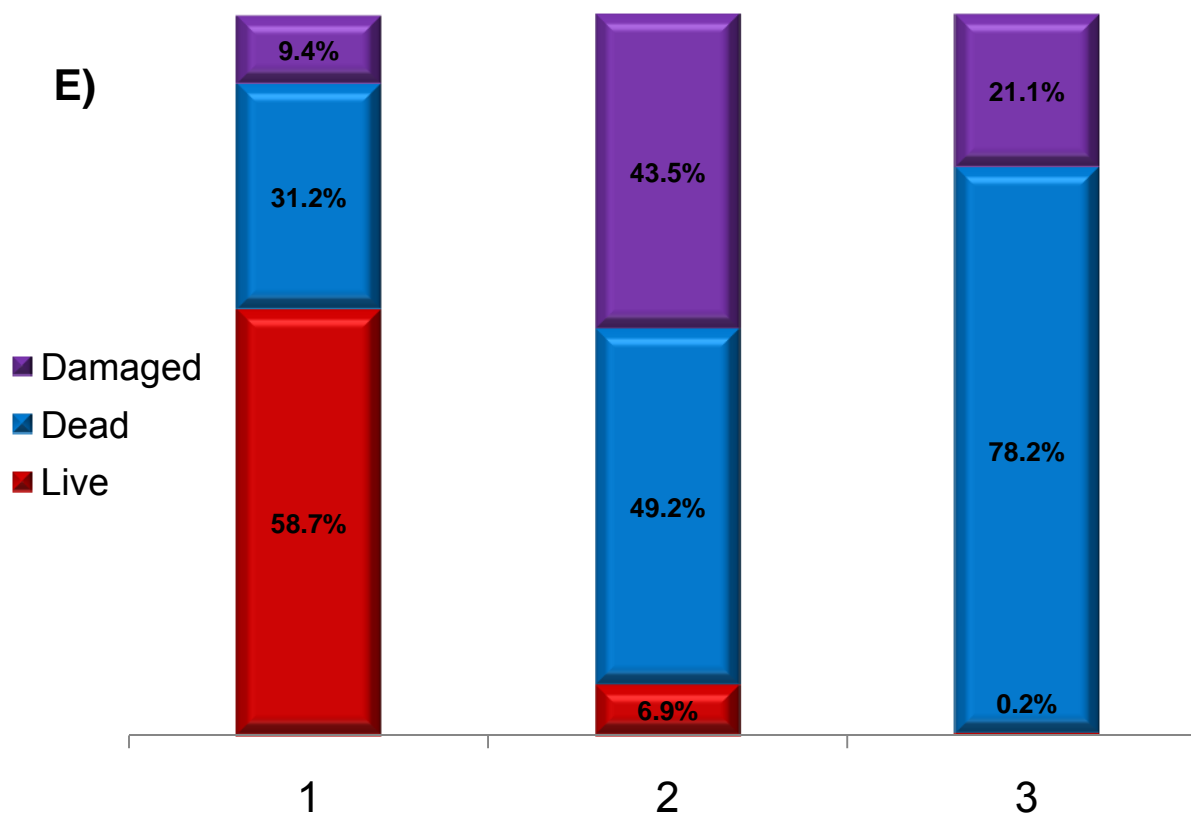
Figure 22: Flow cytometry vitality assay on CHO cells stained with Invitrogen Live/Dead Cell Vitality Kit. Control samples of stained CHO cells are shown in A-1 through D-1. Prior to staining, the cells were A) incubated with TAT-InP/ZnS (10 %) at A-2) 5 nM, A-3) 10 nM, and A-4) 15 nM for 24 h; and B) incubated with TAT-InP/ZnS (100 %) at B-2) 5 nM, B-3) 10 nM, and B-4) 15 nM for 24 h. C) Comparison between (C-1) control and cells transfected with 5 nM of (C-2) TAT-InP/ZnS (10 %) and (C-3) TAT-InP/ZnS (100 %). D) Comparison between (D-1) control and cells transfected with 10 nM of (D-2) TAT-InP/ZnS (10 %) and (D-3) TAT-InP/ZnS (100 %). E) Comparison between (E-1) control and cells transfected with 15 nM of (E-2) TAT-InP/ZnS (10 %) and (E-3) TAT-InP/ZnS (100 %).

Conclusions

Using the small peptide CAAKATAT to passivate the surface of QDs is shown to be a viable method for internalizing QDs into multiple cell types without the use of traditional transfecting agents. The endosomal uptake places the QDs into small, but visible endosomes throughout the cells. Optical images indicate the CPP labeled QDs remain within endosomal vesicles as evidenced by the punctuate images. The cellular uptake efficiency is greatly influenced by the loading level of TAT onto the QDs. The images in Figures 17-19 show that 10 % loading of TAT onto the QD enables

internalization of the TAT-QD while maintaining a healthy cell culture. In Figure 19, however, the internalization of 100 % TAT loaded QDs leads to a cell culture that is greatly disturbed. It has been shown that TAT shows no toxic affects to cells at concentrations up to 50 μM,[64] however, these images suggest that greater concentrations of TAT on the surface of QDs increase their toxicity. Furthermore, it is well known that CdSe/ZnS QDs have toxic effects on cells,[68,99] but the data in Figure 20 shows that for a 24 h transfection time at relatively low concentrations, the CdSe/ZnS QDs have essentially no affect on CHO cells. The same is true for the InP/ZnS QDs regardless of the transfecting mechanism.

At first glance it seems that increasing the concentration of TAT taken into the cells may increase the cytotoxic effects, but further investigation shows it is a much more complex problem.   The flow cytometry data in Figure 21 shows that increasing the concentration of the 100 % TAT loaded QDs greatly increases the susceptibility to staining by membrane impermeant dyes. However, the side-scatter vs. forward-scatter data suggests that this susceptibility is not necessarily due to dying cells. It appears that the increased TAT loading on the QDs begins to overwhelm the membrane surface as the TAT-QD concentration increases, eventually filling the cells with QDs, as seen in Figure 19. This sort of influx of foreign material thrusts the cells into a confused state, unable to perform normal cellular functions, and most likely produces oxidative stress..

The resazurin assay supports the oxidative stress hypothesis, as it is commonly used to indicate which cells in a population are metabolically active by their ability to reduce resazurin to resafurin. This reduction is believed to be accomplished by mitochondrial reductases of healthy, growing cells.[101-102] Metabolically damaged cells would not have these enzymes available to be undergoing metabolic activities, and therefore not be able to reduce the resazurin. If the metabolic damage were purely due to chemical changes within the cells, then we would see the number of "damaged" cells in the treated populations increase linearly as the concentrations of QDs increase. Such is the case for the 10 % TAT loaded QDs. However, the 100 % TAT loaded quantum dots follow a different pattern. Corresponding to the data in Figure 21, at 10 nM, the 100 % TAT loaded QDs overwhelm the cells, leaving all the cells as apparent "dead" cells. For the vitality kit, this means these cells have a compromised membrane

(green staining) and are not able to reduce rezasurin. Considering the microscope images and especially the flow cytometry data in Figure 21B, these cells are more than likely dying, but by a physical mechanism rather than a chemical mechanism. The cells are so full of TAT-QDs that they physically do not have the cytosolic space to undergo metabolic activity.

This conclusion may not be surprising; however, it does confirm that the uptake efficiency and cytotoxicity of TAT-QDs can be directly controlled by the loading level of TAT on the surface of the QDs. More work is needed to find the minimum loading level of TAT that will still allow for uptake of QDs. Additionally, more extensive and better understood metabolic tests should be conducted on treated cells to better understand the relationship between the chemical processes affected by TAT-QDs and the physical hindrance within the cells.   This may be useful in the fine tuning of dosage for different types of drug delivery.

REFERENCES

1. Kamiya, H.; Tsuchiya, H.; Yamazaki, J.; Harashima, H. *Advanced drug delivery reviews* **2001**, *52*, 153.

2. Khalil, I.; Kogure, K.; Akita, H.; Harashima, H. *Pharmacological reviews* **2006**, *58*, 32.

3. Patil, S.; Rhodes, D.; Burgess, D. *The AAPS Journal* **2005**, *7*, 61.

4. Remaut, K.; Sanders, N.; De Geest, B.; Braeckmans, K.; Demeester, J.; De Smedt, S. *Materials Science and Engineering: R: Reports* **2007**, *58*, 117.

5. Wagstaff, K.; Jans, D. *The Biochemical journal* **2007**, *406*, 185.

6. Johnson-Saliba, M.; Jans, D. *Current drug targets* **2001**, *2*, 371.

7. Lechardeur, D.; Lukacs, G. *Current gene therapy* **2002**, *2*, 183.

8. Ludtke, J.; Zhang, G. *Journal of cell science* **1999**, *112*, 2033.

9. Pouton, C. *Advanced drug delivery reviews* **1998**, *34*, 51.

10. Pouton, C.; Wagstaff, K.; Roth, D.; Moseley, G.; Jans, D. *Advanced drug delivery reviews* **2007**, *59*, 698.

11. Sokolova, V.; Epple, M. *Angewandte Chemie (International ed. in English)* **2008**, *47*, 1382.

12. Akerman, M.; Chan, W.; Laakkonen, P.; Bhatia, S.; Ruoslahti, E. *Proceedings of the National Academy of Sciences of the United States of America* **2002**, *99*, 12617.

13. Alivisatos, A.; Gu, W.; Larabell, C. *Annual review of biomedical engineering* **2005**, *7*, 55.

14. Bharali, D.; Lucey, D.; Jayakumar, H.; Pudavar, H.; Prasad, P. *Journal of the American Chemical Society* **2005**, *127*, 11364.

15. Biju, V.; Muraleedharan, D.; Nakayama, K.; Shinohara, Y.; Itoh, T.; Baba, Y.; Ishikawa, M. *Langmuir* **2007**, *23*, 10254.

16. Chakraborty, S.; Fitzpatrick, J.; Phillippi, J.; Andreko, S.; Waggoner, A.; Bruchez, M.; Ballou, B. *Nano Letters* **2007**, *7*, 2618.

17. Chen, B.; Liu, Q.; Zhang, Y.; Xu, L.; Fang, X. *Langmuir* **2008**, *24*, 11866.

18.   Chen, F.; Gerion, D. *Nano Letters* **2004**, *4*, 1827.

19.   Chen, H.; Ho, Y.; Jiang, X.; Mao, H.; Wang, T.; Leong, K. *Molecular therapy: the journal of the American Society of Gene Therapy* **2008**, *16*, 324.

20.   De Koninck, P.; Labrecque, S.; Heyes, C.; Wiseman, P. *HFSP Journal* **2007**, *1*, 5.

21.   de la Fuente, J.; Fandel, M.; Berry, C.; Riehle, M.; Cronin, L.; Aitchison, G.; Curtis, A. *Chembiochem: a European journal of chemical biology* **2005**, *6*, 989.

22.   Delehanty, J.; Mattoussi, H.; Medintz, I. *Analytical and bioanalytical chemistry* **2009**, *393*, 1091.

23.   Delehanty, J.; Medintz, I.; Pons, T.; Dawson, P.; Brunel, F.; Mattoussi, H. *Bioconjugate chemistry* **2006**, *17*, 920.

24.   Derfus, A.; Chan, W.; Bhatia, S. *Advanced Materials* **2004**, *16*, 961.

25.   Derfus, A.; Chen, A.; Min, D.; Ruoslahti, E.; Bhatia, S. *Bioconjugate chemistry* **2007**, *18*, 1391.

26.   Dubach, J.; Harjes, D.; Clark, H. *Journal of the American Chemical Society* **2007**, *129*, 8418.

27.   Gao, X.; Cui, Y.; Levenson, R.; Chung, L.; Nie, S. *Nature biotechnology* **2004**, *22*, 969.

28.   Hoshino, A.; Manabe, N.; Fujioka, K.; Hanada, S.; Yasuhara, M.; Kondo, A.; Yamamoto, K. *Nanotechnology* **2008**, *19*, 495102.

29.   Lagerholm, B.; Wang, M.; Ernst, L.; Ly, D.; Liu, H.; Bruchez, M.; Waggoner, A. *Nano Letters* **2004**, *4*, 2019.

30.   Lei, Y.; Tang, H.; Yao, L.; Yu, R.; Feng, M.; Zou, B. *Bioconjugate chemistry* **2008**, *19*, 421.

31.   Lim, Y.; Lee, E.; Lee, M. *Angewandte Chemie* **2007**, *46*, 9011.

32.   Lin, S.; Xie, X.; Patel, M.; Yang, Y.; Li, Z.; Cao, F.; Gheysens, O.; Zhang, Y.; Gambhir, S.; Rao, J. *BMC Biotechnology* **2007**, *7*, 67.

33.   Liu, W.; Choi, H.; Zimmer, J.; Tanaka, E.; Frangioni, J.; Bawendi, M. *Journal of the American Chemical Society* **2007**, *129*, 14530.

34.   Maysinger, D. *Organic & biomolecular chemistry* **2007**, *5*, 2335.

35. Maysinger, D.; Behrendt, M.; Lalancette-Hébert, M.; Kriz, J. *Nano Letters* **2007**, *7*, 2513.

36. Medintz, I.; Uyeda, H.; Goldman, E.; Mattoussi, H. *Nature materials* **2005**, *4*, 435.

37. Michalet, X.; Pinaud, F.; Bentolila, L.; Tsay, J.; Doose, S.; Li, J.; Sundaresan, G.; Wu, A.; Gambhir, S.; Weiss, S. *Science* **2005**, *307*, 538.

38. Nabiev, I.; Mitchell, S.; Davies, A.; Williams, Y.; Kelleher, D.; Moore, R.; Gun'ko, Y.; Byrne, S.; Rakovich, Y.; Donegan, J.; Sukhanova, A.; Conroy, J.; Cottell, D.; Gaponik, N.; Rogach, A.; Volkov, Y. *Nano Letters* **2007**, *7*, 3452.

39. Nan, X.; Sims, P.; Chen, P.; Xie, X. *The journal of physical chemistry. B* **2005**, *109*, 24220.

40. Ozkan, M. *Drug discovery today* **2004**, *9*, 1065.

41. Prow, T.; Smith, J.; Grebe, R.; Salazar, J.; Wang, N.; Kotov, N.; Lutty, G.; Leary, J. *Molecular vision* **2006**, *12*, 606.

42. Rajan, S.; Vu, T. *Nano Letters* **2006**, *6*, 2049.

43. Riegler, J.; Ditengou, F.; Palme, K.; Nann, T. *Journal of Nanobiotechnology* **2008**, *6*, 7.

44. Ruan, G.; Agrawal, A.; Marcus, A.; Nie, S. *Journal of the American Chemical Society* **2007**, *129*, 14759.

45. Santra, S.; Yang, H.; Holloway, P.; Stanley, J.; Mericle, R. *Journal of the American Chemical Society* **2005**, *127*, 1656.

46. Silver, J.; Ou, W. *Nano Letters* **2005**, *5*, 1445.

47. Smith, A.; Duan, H.; Mohs, A.; Nie, S. *Advanced drug delivery reviews* **2008**, *60*, 1226.

48. Srinivasan, C.; Lee, J.; Papadimitrakopoulos, F.; Silbart, L.; Zhao, M.; Burgess, D. *Molecular Therapy* **2006**, *14*, 192.

49. Susumu, K.; Uyeda, H.; Medintz, I.; Pons, T.; Delehanty, J.; Mattoussi, H. *Journal of the American Chemical Society* **2007**, *129*, 13987.

50. Tekle, C.; Deurs, B.; Sandvig, K.; Iversen, T. *Nano Letters* **2008**, *8*, 1858.

51. Wei, Y.; Jana, N.; Tan, S.; Ying, J. *Bioconjugate chemistry* **2009**, *20*, 1752.

52. Xue, F.; Chen, J.; Guo, J.; Wang, C.; Yang, W.; Wang, P.; Lu, D. *Journal of fluorescence* **2007**, *17*, 149.

53. Yezhelyev, M.; Qi, L.; O'Regan, R.; Nie, S.; Gao, X. *Journal of the American Chemical Society* **2008**, *130*, 9006.

54. Yong, K.; Ding, H.; Roy, I.; Law, W.; Bergey, E.; Maitra, A.; Prasad, P. *ACS nano* **2009**.

55. Yum, K.; Na, S.; Xiang, Y.; Wang, N.; Yu, M. *Nano Letters* **2009**, *9*, 2193.

56. Zhang, Y.; So, M.; Rao, J. *Nano Letters* **2006**, *6*, 1988.

57. Choi, H.; Liu, W.; Misra, P.; Tanaka, E.; Zimmer, J.; Itty, I.; Bawendi, M.; Frangioni, J. *Nature biotechnology* **2007**, *25*, 1165.

58. Aldana, J.; Lavelle, N.; Wang, Y.; Peng, X. *Journal of the American Chemical Society* **2005**, *127*, 2496.

59. Duan, H.; Nie, S. *Journal of the American Chemical Society* **2007**, *129*, 3333.

60. Li, D.; Li, G.; Guo, W.; Li, P.; Wang, E.; Wang, J. *Biomaterials* **2008**, *29*, 2776.

61. Ghosh, P.; Han, G.; De, M.; Kim, C.; Rotello, V. *Advanced drug delivery reviews* **2008**, *60*, 1307.

62. Han, G.; Chari, N.; Verma, A.; Hong, R.; Martin, C.; Rotello, V. *Bioconjugate chemistry* **2005**, *16*, 1356.

63. Zelphati, O.; Szoka Jr, F. *Proceedings of the National Academy of Sciences of the United States of America* **1996**, *93*, 11493.

64. El-Andaloussi, S.; Järver, P.; Johansson, H.; Langel, Ü. *The Biochemical journal* **2007**, *407*, 285.

65. Futaki, S.; Goto, S.; Suzuki, T.; Nakase, I.; Sugiura, Y. *Current protein & peptide science* **2003**, *4*, 87.

66. Hassane, F.; Saleh, A.; Abes, R.; Gait, M.; Lebleu, B. *Cellular and molecular life sciences: CMLS* **2009**.

67. Nitin, N.; LaConte, L.; Rhee, W.; Bao, G. *Annals of biomedical engineering* **2009**, *37*, 2018.

68. Kirchner, C.; Liedl, T.; Kudera, S.; Pellegrino, T.; Muñoz, J.; Gaub, H.; Stölzle, S.; Fertig, N.; Parak, W. *Nano Letters* **2005**, *5*, 331.

69.   Kabe, I.; Omae, K.; Nakashima, H.; Nomiyama, T.; Uemura, T.; Hosoda, K.; Ishizuka, C.; Yamazaki, K.; Sakurai, H. *Journal of Occupational Health* **1996**, *38*, 6.

70. Oda, K. *Industrial health* **1997**, *35*, 61.

71. Yamazaki, K.; Tanaka, A.; Hirata, M.; Omura, M.; Makita, Y.; Inoue, N.; Sugio, K.; Sugimachi, K. *Journal of Occupational Health* **2000**, *42*, 169.

72.   Gerbec, J.; Magana, D.; Washington, A.; Strouse, G. *Journal of the American Chemical Society* **2005**, *127*, 15791.

73. Lovingood, D.; Strouse, G. *Nano Letters* **2008**, *8*, 3394.

74. Xie, R.; Battaglia, D.; Peng, X. *Journal of the American Chemical Society* **2007**, *129*, 15432.

75. Murray, C.; Sun, S.; Gaschler, W.; Doyle, H.; Betley, T.; Kagan, C. *IBM Journal of Research and Development* **2001**, *45*, 47.

76. West, K.; Otto, S. *Current drug discovery technologies* **2005**, *2*, 123.

77.   Clapp, A.; Medintz, I.; Mattoussi, H. *Chemphyschem: a European journal of chemical physics and physical chemistry* **2006**, *7*, 47.

78. Ewert, K.; Slack, N.; Ahmad, A.; Evans, H.; Lin, A.; Samuel, C.; Safinya, C. *Current medicinal chemistry* **2004**, *11*, 133.

79. Karmali, P.; Chaudhuri, A. *Medicinal research reviews* **2007**, *27*, 696.

80.   Medintz, I.; Clapp, A.; Mattoussi, H.; Goldman, E.; Fisher, B.; Mauro, J. *Nature materials* **2003**, *2*, 630.

81. Singh, M.; Jennings, T.; Strouse, G. *The journal of physical chemistry. B* **2009**, *113*, 552.

82.   Zhou, D.; Piper, J.; Abell, C.; Klenerman, D.; Kang, D.; Ying, L. *Chemical Communications* **2005**, 4807.

83. Jiang, W.; Mardyani, S.; Fischer, H.; Chan, W. *Chemistry of Materials* **2006**, *18*, 872.

84. 33mer: 5'(RSSC6) CTC CGC CTA CCG AAT TCG ATA GTC ATC CAC ATG -3'
33mer: 5' (C6 Amino) CTC CGC CTA CCG AAT TCG ATA GTC ATC CAC ATG -3'
29mer: 5' TG GAT GAC TAT CGA ATT CGG TAG GCG GAG 3'.

85. Godbey, W.; Wu, K.; Mikos, A. *Proceedings of the National Academy of Sciences of the United States of America* **1999**, *96*, 5177.

86. Goldman, E.; Medintz, I.; Hayhurst, A.; Anderson, G.; Mauro, J.; Iverson, B.; Georgiou, G.; Mattoussi, H. *Analytica Chimica Acta* **2005**, *534*, 63.

87. Hansma, H.; Laney, D. *Biophysical Journal* **1996**, *70*, 1933.

88. Hud, N.; Polak, M. *Current opinion in structural biology* **2001**, *11*, 293.

89. Koltover, I.; Wagner, K.; Safinya, C. *Proceedings of the National Academy of Sciences of the United States of America* **2000**, *97*, 14046.

90. Mahtab, R.; Sealey, S.; Hunyadi, S.; Kinard, B.; Ray, T.; Murphy, C. *Journal of inorganic biochemistry* **2007**, *101*, 559.

91. Algar, W.; Krull, U. *Langmuir* **2008**, *24*, 5514.

92. Guo, R.; Song, Y.; Wang, G.; Murray, R. *Journal of the American Chemical Society* **2005**, *127*, 2752.

93. Lecoeur, H. *Experimental cell research* **2002**, *277*, 1.

94. Ormerod, M.; Sun, X.; Snowden, R.; Davies, R.; Fearnhead, H.; Cohen, G. *Cytometry* **1993**, *14*, 595.

95. Andree, H.; Reutelingsperger, C.; Hauptmann, R.; Hemker, H.; Hermens, W.; Willems, G. *The Journal of biological chemistry* **1990**, *265*, 4923.

96. Fadok, V.; Voelker, D.; Campbell, P.; Cohen, J.; Bratton, D.; Henson, P. *Journal of immunology* **1992**, *148*, 2207.

97. Marquis, B.; Love, S.; Braun, K.; Haynes, C. *The Analyst* **2009**, *134*, 425.

98. van Engeland, M.; Nieland, L.; Ramaekers, F.; Schutte, B.; Reutelingsperger, C. *Cytometry* **1998**, *31*, 1.

99. Hoshino, A.; Fujioka, K.; Oku, T.; Suga, M.; Sasaki, Y.; Ohta, T.; Yasuhara, M.; Suzuki, K.; Yamamoto, K. *Nano Letters* **2004**, *4*, 2163.

100. Krysko, D.; Vanden, B.; D'Herde, K.; Vandenabeele, P. *Methods* **2008**, *44*, 205.

101. Anoopkumar-Dukie, S.; Carey, J.; Conere, T.; O'sullivan, E.; van Pelt, F.; Allshire, A. *The British journal of radiology* **2005**, *78*, 945.

102. O'Brien, J.; Wilson, I.; Orton, T.; Pognan, F. *European journal of biochemistry/FEBS* **2000**, *267*, 5421.

BIOGRAPHICAL SKETCH

I am a Captain the United States Air Force and have served six years as a chemist. I received my bachelor's degree in Biochemistry from the United States Air Force Academy in 2004. Since then, I have worked as a program manager for various AF projects. I was chosen by the Air Force to participate in a graduate program that included obtaining a master's degree from a civilian institution followed by a teaching position at the Air Force Academy. This is how I was able to complete this degree.